Adsorption
https://doi.org/10.1007/s10450-024-00523-1

Competitive Adsorption Studies of $MgFe_2O_4$-Biochar Nanocomposites for the Removal of Chromium and Nickel Ions in Single and Binary Metal Ion System

Gautham Kurup[1,2] · Neeraj Krishnan[1,2] · Vaishnav M. R.[1,2] · Roopak A. R.[1,2] · K. Nithya[1,2] · Asha Sathish[3,4] · Selvaraju Sivamani[5] · Aswathy S. Cheruvally[1,2]

Received: 18 May 2024 / Revised: 5 July 2024 / Accepted: 14 July 2024

Abstract

The presence of heavy metal ions in water bodies constitutes a significant environmental hazard. The development of sustainable and cost-effective adsorbent materials for their removal is an urgent priority. In alignment with this critical objective, the present study explores the potential of a novel composite material for water remediation. This composite, fabricated from biochar and magnesium ferrite nanoparticles, targets the removal of hexavalent chromium and divalent nickel. While prior research has explored the application of rice husk as an adsorbent, no investigation, to our knowledge, has examined the potential of magnesium ferrite-rice husk composites for this purpose. Initial screening identified the biochar-magnesium ferrite composite (pre-calcination) as the most effective adsorbent. This composite displayed a superior surface area (151 m^2/g) compared to calcined magnesium ferrite (91 m^2/g) and achieved exceptional removal efficiencies for both chromium (50 mg/g) and nickel (54 mg/g). Optimal chromium removal occurred at pH 1 with a 110-minute contact time, while nickel favored a pH of 6 and the same contact time. The adsorption process was characterized as physisorption and endothermic. Notably, the composite exhibited efficient regeneration (82% for nickel and 90% for chromium) using simple acid/base solutions. The BJH analysis of pore characteristics indicated an average pore diameter of 1.5365 nm and a total pore volume of 0.17 cm^3/g. The research findings demonstrate the composite's effectiveness as a sustainable adsorbent for capturing heavy metal ions from water.

✉ K. Nithya
k_nithya@cb.amrita.edu

[1] Department of Chemical Engineering and Materials Science, Amrita School of Engineering, Amrita Vishwa Vidyapeetham, Coimbatore 641112, India

[2] Centre of Excellence in Advanced Materials and Green Technologies (CoE-AMGT), Amrita School of Engineering, Amrita Vishwa Vidyapeetham, Coimbatore 641112, India

[3] Department of Sciences, Amrita School of Physical Sciences, Amrita Vishwa Vidyapeetham, Coimbatore, Tamil Nadu 641112, India

[4] Functional Materials Laboratory, Amrita School of Engineering, Amrita Vishwa Vidyapeetham Coimbatore 641112, India

[5] Engineering Department, University of Technology and Applied Sciences (Salalah College of Technology), Salalah, Oman

Graphical Abstract

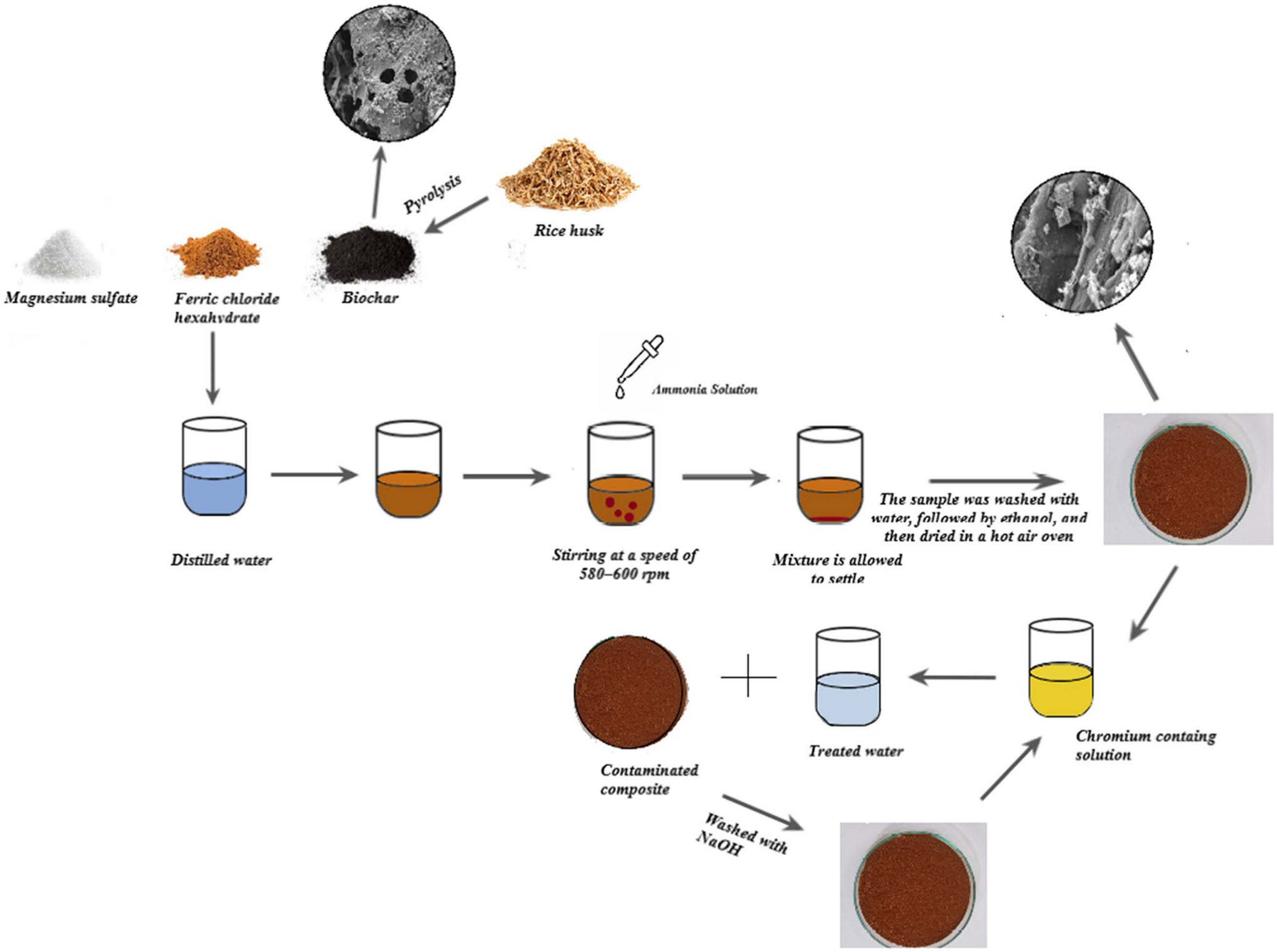

Keywords Chromium · Nickel · Rice husk · Magnesium ferrite · Adsorption

1 Introduction

Heavy metal ions represent a perilous, persistent, and non-biodegradable pollutant found in industrial effluents. The surge in global industrial manufacturing capacity, escalating from 1.2 billion tons in 2000 to 2.3 billion tons in 2017, is a direct outcome of the fourth industrial revolution. Consequently, this heightened manufacturing capacity has resulted in an increased release of industrial effluents that contain heavy metal ions, into water sources [3]. The industries contributing substantial amounts of metals to wastewater encompass a wide range of sectors. These include chemical production, sugar refineries, food and dairy processing, paper and pulp mills, textile bleaching and dyeing facilities, mining and quarries, battery manufacturing units, nuclear power plants, organic chemical production sites, leather and tannery operations, iron and steel manufacturing plants, soap and detergent industries, electric power plants, metal refining facilities, pesticide and biocide manufacturing sites, petroleum and petrochemical refineries, pharmaceutical manufacturing units, metal processing facilities, and electroplating industries. Together, these diverse sectors play a significant role in introducing metal pollutants into wastewater [9].

Though present in trace amounts in wastewater, chromium, nickel, cadmium, lead, copper, mercury and other heavy metals, pose health and environmental risks due to their toxicity and persistence. Resisting metabolic breakdown, they accumulate in soft tissues, causing severe health hazards. Their non-biodegradable nature heightens concerns about lasting environmental impact, emphasizing the critical need for efficient wastewater treatment to mitigate harm to ecosystems. Hexavalent chromium has been demonstrated to exhibit mutagenic and carcinogenic properties in both humans and animals. The widespread industrial use of hexavalent chromium, coupled with its high toxicity and mobility, has led to its infamy in the realm of environmental pollution [30]. Hexavalent chromium exists as H_2CrO_4, $HCrO_4^-$, CrO_4^{2-} and $Cr_2O_7^{2-}$ in the aqueous solution [20]. As outlined by the Central Pollution Control Board (CPCB) and the U.S. Environmental Protection Agency (USEPA), acceptable concentrations of hexavalent chromium in effluents are set at 0.01 mg/L for potable water and 0.1 mg/L for industrial effluents [19]. At elevated concentrations, divalent nickel, while non-toxic in low amounts, has been linked to health issues such as contact dermatitis, cardiovascular diseases, respiratory tract cancer, kidney diseases, and lung fibrosis. The World Health Organization (WHO) has set the maximum allowable level of nickel in drinking water at 0.02 mg/L [18].

A variety of methods such as chemical precipitation, solvent extraction, ion exchange, advanced oxidation, flocculation, electrochemical treatment, electrodialysis, membrane filtration, reverse osmosis, and adsorption have been reported in the separation of heavy metal ions [31]. Many of the aforementioned metal ion removal methods suffer from significant drawbacks. One primary issue is the substantial generation of sludge during treatment, posing challenges in both handling and disposal. Furthermore, the effectiveness of these methods is compromised, particularly in removing metal ions at low concentrations. This limitation is crucial as many industrial effluents and contaminated water sources contain trace amounts of metal ions that may go unaddressed. Additionally, these methods often demand high energy inputs, contributing to elevated operational costs and environmental concerns. The overall operational and maintenance costs associated with these methods are also high, making them less economically viable. Perhaps most concerning is the lack of sustainability in these approaches, raising questions about their long-term environmental impact. Considering these drawbacks, there is a pressing need to explore and develop alternative methods that offer more efficient and sustainable solutions for metal ion removal. Adsorption proves to be a highly advantageous alternative, primarily owing to its operational flexibility, cost-effectiveness, and capability to achieve a high-efficiency process for generating treated effluents of superior quality. Furthermore, its efficacy extends to addressing a diverse range of target contaminants, making it a versatile and reliable method in the realm of water treatment [7].

Researchers are actively working on the creation of cost-efficient and highly effective adsorbents for wastewater treatment, with biochar emerging as a notable contender in this regard. Biochar, a porous carbonaceous substance, is formed through the thermochemical breakdown of biomass feedstock, often in the absence of oxygen. Biomass feedstock encompasses various organic waste materials such as crop residues, wood chips, algae, sewage sludge, manures, and organic municipal solid wastes. The appeal of biochar lies in its dual advantages: firstly, the production of biochar can serve to counteract greenhouse gas emissions by securely storing carbon, thus preventing the release of these gases into the atmosphere during biomass degradation. Secondly, biochar stands out as an efficient, cost-effective, and environmentally friendly adsorbent, attributed to its sizable surface area and plentiful surface functional groups [29]. Biochar derived from rice husk possesses significant potential as an adsorbent for the removal of heavy metal ions. This potential stems from the abundant floristic fiber in rice husk, coupled with the presence of various functional groups like hydroxyl, carboxyl, and amidogen. These inherent characteristics make the process of adsorption highly feasible. Furthermore, biochar produced from rice husk has been documented to exhibit diverse functions and is recognized as a cost-effective material for this purpose [21].

Nanomaterials are frequently integrated into biochar due to their ability to enhance surface area, high-affinity adsorption sites, thermal stability, and cation exchange capacity [24]. Magnetic spinel ferrites have gained significant popularity for the removal of hazardous contaminants from water in recent years. The spinel crystal structure is characterized by the AB_2O_4 formula, where A and B represent cations in tetrahedral and octahedral sites, respectively. An added advantage of these ferrites is their ease of removal from the aqueous environment through the application of a magnetic field [26].

The primary objective of this research is to assess the adsorption capabilities of biochar derived from rice husk, specifically focusing on a modified biochar. This modified biochar is utilized for adsorbing chromium and nickel ions, with potential applications in wastewater treatment. What sets this study apart is that while previous research has explored the adsorption abilities of rice husk biochar [8], no investigations have yet examined the potential of the $MgFe_2O_4$ rice husk biochar nanocomposite. The novelty lies in investigating the unexplored potential of the $MgFe_2O_4$ rice husk biochar nanocomposite. No prior studies have examined its effectiveness in heavy metal adsorption. This research is the first to explore its capabilities, opening doors for a potentially more efficient and selective adsorbent compared to traditional biochar. The study meticulously investigates the impact of various factors—such as concentration, time,

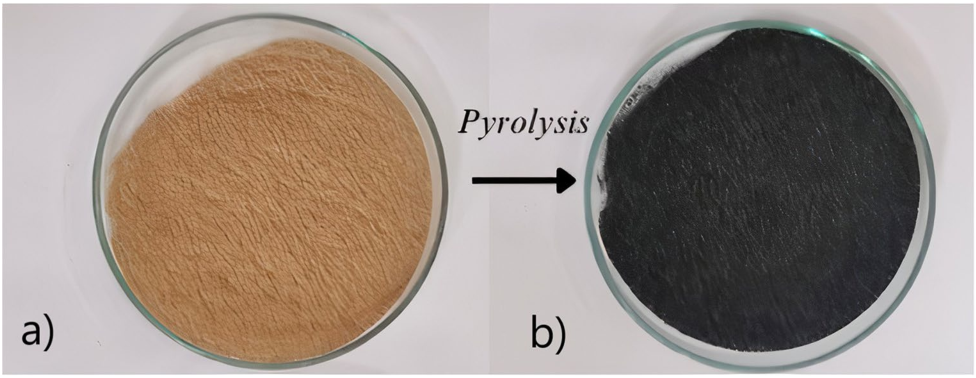

Fig. 1 (**a**) Powdered Rice Husk (**b**) Powdered Rice Husk Biochar

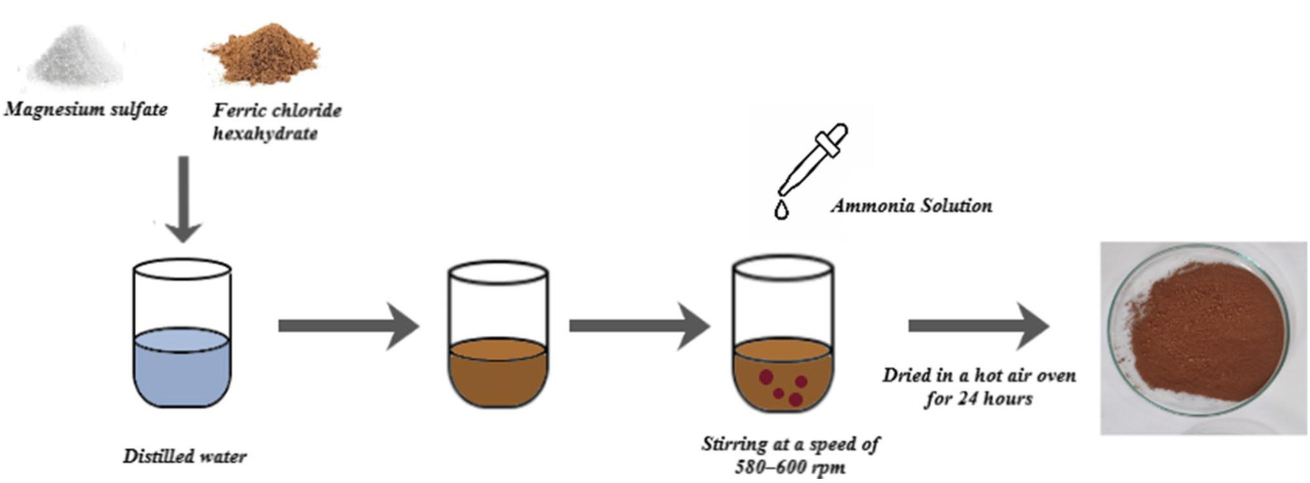

Fig. 2 Preparation of MgFe Nanoparticles

and temperature—on the adsorption process, contributing to the field's understanding of this novel material.

2 Materials and methods

2.1 Procurement of materials

Magnesium Sulphate (99% Purity, Molecular Weight 246.48 g mol^{-1}), Ferric Chloride Hexahydrate (99% Purity, Molecular Weight 270.33 g mol^{-1}), Ammonia Buffer solution, Ethanol (99% Purity, Molecular Weight 35.05 g mol^{-1}), Hydrochloric acid (99% Purity, Molecular Weight 36.46 g mol^{-1}), and Sodium Hydroxide (2.13 g cm^{-3}, Molecular Weight 40 g mol^{-1}) were obtained from Nice Chemicals Pvt. Ltd., and glassware was obtained from Borosil Pvt. Ltd. The rice husk was obtained from a nearby rice mill.

2.2 Preparation of biochar

In the process of biochar preparation, rice husk was chosen as biomass as shown in Fig. 1. The optimal temperature and duration for pyrolysis were determined through multiple trials. Pyrolysis was carried out at 400°C for 30 min using a muffle furnace equipped with a mounted vent condenser. The resulting biochar exhibited a reduction in weight due to the vaporization of all organic volatiles present in the biomass as shown in Fig. 1.

2.3 Preparation of MgFe (Magnesium Ferrite)

To prepare MgFe, 2.5 g of magnesium sulfate and 5.4 g of ferric chloride hexahydrate were dissolved in 100 ml of distilled water as shown in Fig. 2. The solution was subjected to magnetic stirring for 30 min at a temperature within the range of 60–70 °C and a stirring speed of 580–600 rpm. Subsequently, 30 mL of ammonia solution was added drop by drop over 40 min. The pH of the solution, initially at 12, was adjusted to 7 during this process. The resulting mixture was then dried in a hot air oven for 24 h, yielding approximately 2 g of MgFe. For further enhancement, the MgFe was subjected to calcination in a muffle furnace for 4 h at 500 °C to optimize its properties for adsorption studies.

2.4 Preparation of B-MgFe-BC (Biochar-Magnesium Ferrite composite before calcination) and B-MgFe-AC (Biochar-Magnesium Ferrite composite after calcination)

For the preparation of the B-MgFe-BC, a conical flask was employed to combine 2.5 g of magnesium sulfate, 5.4 g of ferric chloride hexahydrate, and 0.5 g of biochar in 100 ml of distilled water as shown in Fig. 3. A magnetic pellet was introduced into the mixture and stirred using a magnetic stirrer operating at a speed of 580–600 rpm within a temperature range of 60–70 °C. After a 30-minute interval, ammonia solution was gradually added over 40 min. Following the stirring process, the magnetic pellet was removed, and the mixture was allowed to settle. Water washing was performed at intervals of 15–20 min until the pH of the mixture decreased from 12 to 7. Upon reaching a pH of 7, ethanol washing was carried out to remove impurities present in the mixture. Subsequently, the mixture was dried in a hot air oven for approximately 24 h, resulting in the obtainment of around 2.5 g of the B-MgFe-BC. To further enhance its properties for adsorption studies, the B-MgFe-BC underwent calcination in a muffle furnace for 4 h at 500°C.

2.5 Characterization

The synthesized adsorbents, MgFe-BC, MgFe-AC, B-MgFe-BC, and B-MgFe-AC, composed of magnetite nanoparticles, underwent a detailed characterization using multiple analytical techniques to elucidate their structural and chemical attributes. The samples were characterized by several instruments. Functional group analysis was attained by Fourier transform infrared spectrometer (FTIR, Nexus 470, Nicolet, USA) between wavelengths of 400–5000 cm^{-1} with 32 scans at room temperature and a resolution of 4 cm^{-1}. The morphological properties were obtained by field emission scanning electron microscopy (SEM, EDS, Hitachi 5V5000, Hitachi Hi-Tech Co., Ltd.) at the voltage of 5 kV and 15 kV. Thermogravimetric curves were obtained by the thermogravimetric analyzer (TGA, SDT Q600, TA Instrument) at a 10 ºC·min^{-1} heating rate in the range from 20 ºC to 800 ºC in the 100 mL·min^{-1} atmosphere of nitrogen. The specific surface properties were examined by the Specific surface area analyzer (BET, ASAP 2460, McMuritik, USA).

2.6 Batch experiments

A stock solution of hexavalent chromium at a concentration of 1000 ppm was prepared by dissolving 2.8 g of potassium dichromate in 1000 ml of demineralized water at room temperature using a standard measuring flask. Similarly, a 1000 ppm solution of bivalent nickel was created by dissolving 4.5 g of nickel Sulfate hexahydrate in 1000 ml of demineralized water, also at room temperature and in a standard measuring flask. All batch studies conducted in this research were executed in a benchtop incubator shaker operating at 150 rpm.

To identify the most promising adsorbent, we initially compared five candidates: Biochar, MgFe-BC, MgFe-AC, B-MgFe-BC, and B-MgFe-AC. Based on this screening, B-MgFe-BC was chosen for further investigation due to its superior adsorption potential. This in-depth analysis allows for a more refined understanding of B-MgFe-BC's efficacy and paves the way for future optimization. Various chromium and nickel solutions (50–500 ppm) were prepared to study concentration effects, including mixed solutions. The experiment monitored adsorption efficiency over 120 min (10-minute intervals) and also at different temperatures (room temperature to 60 °C) using 0.5 g of adsorbent. Atomic absorption spectrometry (AAS) quantified the remaining Cr(VI) and Ni(II) ions. The values of the limit of detection (LoD) of chromium and nickel are 0.0001 and 0.0004 mg/L respectively. On the other hand, the limits of quantitation (LoQ) for chromium and nickel are 0.001 and 0.005 mg/L respectively.

Assessment of adsorption efficiency involved calculating the percentage difference between initial and final solution

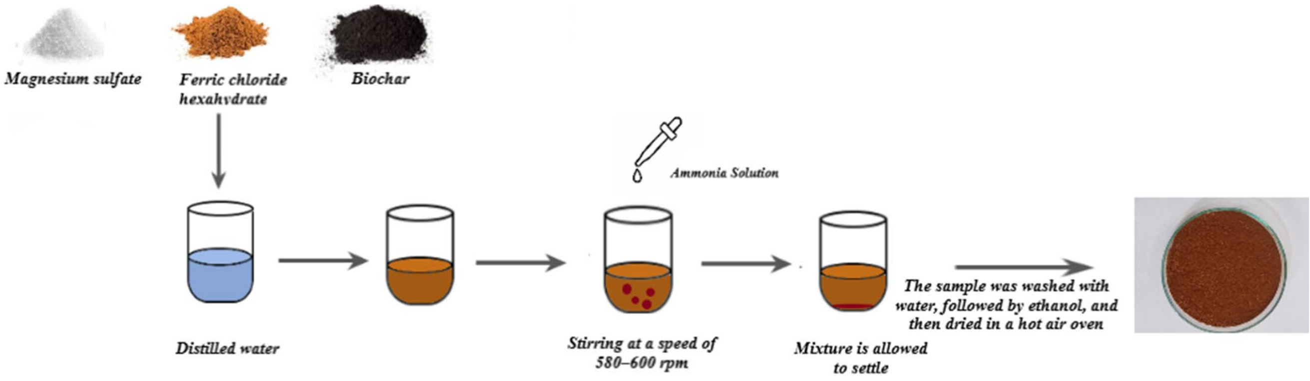

Fig. 3 Preparation of B-MgFe-BC Composites

concentrations, divided by the initial solution concentration and then multiplied by one hundred. Adsorption capacity determination was achieved by calculating the difference between initial and final solution concentrations, dividing by the mass of the adsorbent in grams, and multiplying by the volume of the solution expressed in liters. Concentration values were reported in milligrams per liter (mg/L), while adsorption capacity was expressed in milligrams per gram (mg/g) [12].

For understanding reaction kinetics, kinetic models were formulated using data obtained from batch experiments. Equilibrium for adsorption and adsorption capacity was explored through isotherms, including Langmuir, Freundlich, Temkin and Dubinin-Radushkevich isotherms, and thermodynamic studies were conducted to discern whether the removal process was endothermic or exothermic. The adsorbent's reusability was confirmed through regeneration studies. Desorption experiments, using NaOH and HCl as the eluting agent, provided insights into the adsorption mechanism by evaluating the potential of both physical and chemical adsorption. The efficiency of desorption was calculated by determining the ratio of released metal ion concentration to initially sorbed metal ion concentration, multiplied by a hundred.

3 Results and discussion

3.1 Characterization

3.1.1 Identification of the functional groups

The FTIR spectra of the four adsorbents, namely MgFe-BC, MgFe-AC, B-MgFe-BC, and B-MgFe-AC, exhibit distinctive features as shown in Fig. 4. In the FTIR spectrum of MgFe-BC, a relatively weak adsorption band at 441.35 cm^{-1} indicates the stretching vibration of the M-O bond at octahedral sites, while a robust line at 692.47 cm^{-1} is attributed to the M-O stretching vibration at tetrahedral sites. The faint peak at 1643.87 cm^{-1} results from the O-H bending vibration mode, indicating the presence of both free and absorbed water. A strong peak at 1102 cm^{-1} corresponds to the stretching vibration of the C-O bond, and a medium adsorption band at 1368 cm^{-1} represents the bending vibration of the C-H bond. In the FTIR spectrum of MgFe-AC,

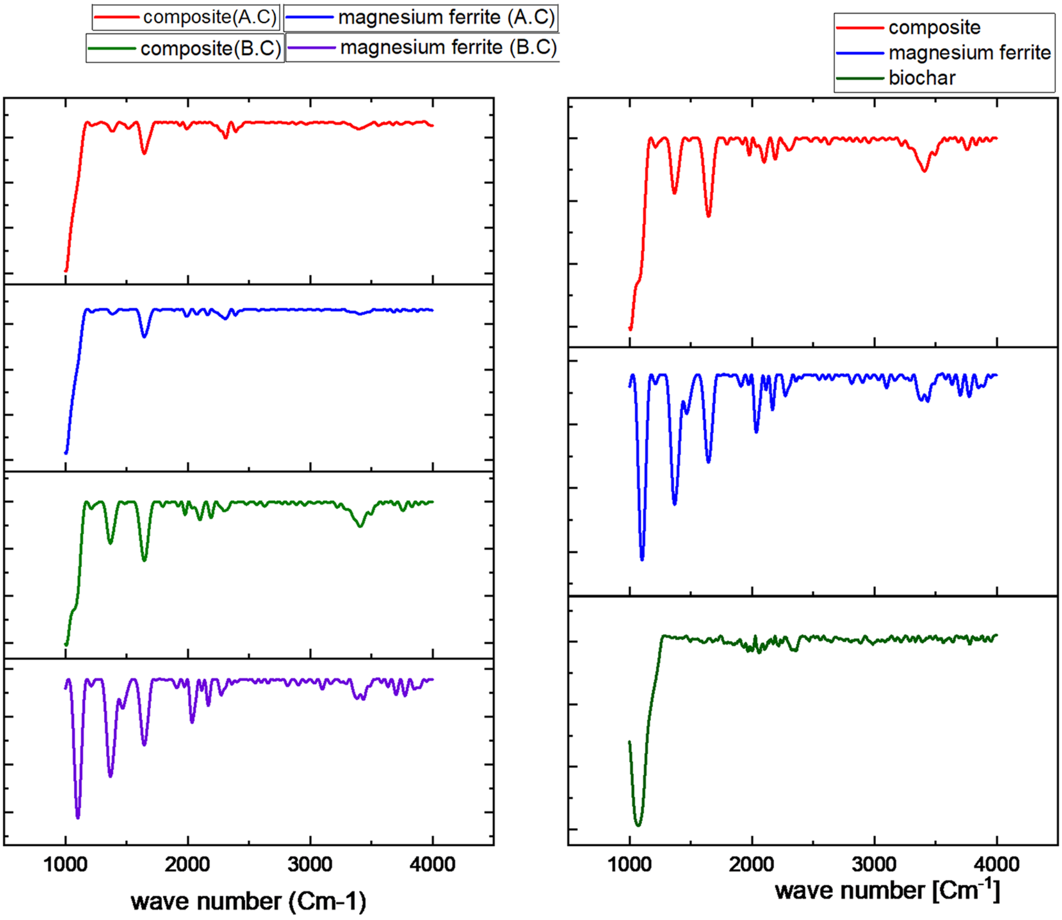

Fig. 4 FTIR spectra MgFe-BC, MgFe-AC, B-MgFe-BC, B-MgFe-AC and Biochar

the same bonds found in MgFe-BC are present. The O-H bending vibration mode is observed at 1644.06 cm_{-1}, and the strong bending vibration of the C-O bond has shifted to 1004.77 cm^{-1}. Two prominent adsorption bands at 579 cm^{-1} and 449.78 cm^{-1} indicate the stretching vibration of the M-O bond at tetrahedral and octahedral sites, respectively, supporting the confirmation of the spinel structure of the MgFe adsorbent.

The FTIR spectra of B-MgFe-BC reveal adsorption peaks similar to MgFe-BC, with peaks at 1645.41 cm^{-1} and 1367.19 cm^{-1} corresponding to the O-H bond's bending vibration and C-H bond's bending vibration respectively. At 1007.26 cm^{-1}, the bending vibration of the C-O bond is indicated. Peaks at 688.45 cm^{-1} and 438.84 cm^{-1} correspond to the stretching vibration of the M-O bond at tetrahedral and octahedral sites, respectively. The presence of a peak at 465.02 cm^{-1} suggests a SiO_2 bond and a band at 715 cm^{-1} indicates the presence of a C-H bond.

Similarly, the FTIR spectra of B-MgFe-AC display adsorption peaks akin to those found in MgFe-AC. The O-H bending vibration at 1644.47 cm^{-1} mirrors B-MgFe-AC and the robust C-O band is found at 1003 cm^{-1}. Two significant adsorption bands at 585 cm^{-1} and 448.20 cm^{-1} indicate high-frequency stretching vibrations of the M-O bond at tetrahedral and low-frequency M-O stretching vibrations at octahedral sites, affirming the spinel structure of MgFe.

In all four adsorbents, MgFe-BC, MgFe-AC, B-MgFe-BC, and B-MgFe-AC, distinct bands in the high-frequency range (650–530 cm^{-1}) and low-frequency range (446–400 cm^{-1}) are observed. The higher frequency band is attributed to the stretching intrinsic vibration of the spinel unit cell in the tetrahedral site, while the lower band is caused by the stretching vibration of metal-oxygen in the octahedral (B) site, characteristic of the spinel structure of MgFe. [14].

The FTIR spectra of B-MgFe-AC and B-MgFe-BC were compared with the FTIR spectrum of biochar, as depicted in Fig. 4. In the biochar spectrum, the 1,701 cm^{-1} band was assigned to the carboxyl group (C = O), the 1,600 cm^{-1} band corresponded to the stretching vibration of C = C in aromatic groups, and the 795 cm^{-1} band confirmed the vibration of the aromatic C-H bond. The aromatic structure is thought to generate π-electrons capable of forming strong bonds with heavy metal ions. Additionally, the biochar FTIR spectra displayed a significant band at 1,072 cm^{-1}, associated with the vibration of Si-O-Si, and a band at 462.05 cm^{-1}, suggesting the presence of a SiO_2 bond. The presence of these identical bonds in B-MgFe-AC and B-MgFe-BC suggests the successful integration of biochar with MgFe, maintaining the integrity of the biochar matrix without altering its primary functional groups [25].

FTIR analysis of the adsorbent revealed the identification of functional groups, each playing a vital role in the capture of chromium and nickel ions. Carboxyl groups (C = O) attract and exchange ions on the adsorbent surface while C = C groups, depending on their arrangement, can create a weak but helpful interaction with the metal ions through a pi-electron cloud. While C-H groups don't directly bind the metals, they influence the overall hydrophobicity (water repellency) of the adsorbent, which can be crucial for selective adsorption. The presence of silica, indicated by the Si-O-Si bond, is a common feature in many adsorbents. Silica provides structural stability and a larger surface area - both essential for efficient adsorption. Additionally, O-H groups participate in hydrogen bonding with the metal ions, offering another avenue for capture. C-O bonds, depending on their specific context (alcohols, ethers, etc.), can contribute to hydrogen bonding or influence the overall surface chemistry, playing a more subtle role. The most significant finding, however, is the M-O bond. This suggests the presence of metal oxides on the adsorbent surface, acting as highly effective binding sites for strong interaction with chromium and nickel ions. Furthermore, the intensity of each peak in the FTIR spectrum revealed the relative abundance of these functional groups, providing valuable insights into their contribution to the overall adsorption mechanism. By understanding these functionalities, we can gain a deeper understanding of how the adsorbent captures and holds onto these metal ions.

3.1.2 Thermogravimetric analysis

The experimental Thermogravimetric Analysis (TGA) findings are depicted in Fig. 5(a) for biochar, MgFe-AC, and B-MgFe-BC. These visual representations showcase the weight loss profiles and the derivative weight loss (DTG) of the specimens, all subjected to temperature variations from 30 °C to 800 °C (Fig. 5(b)). Within this temperature range, two prominent phases of mass reduction emerge consistently across all examined samples, namely MgFe-AC and B-MgFe-BC. The initial phase is attributed to the volatilization of water and certain gases adsorbed on the surface. The subsequent phase is linked to the disintegration of organic matter. Notably, the absence of mass loss and the presence of a plateau region beyond 650 °C suggest the decomposition of spinel ferrite into other compounds like α–Fe_2O_3 and MgO. This transformation is indicated in the TGA profiles, underscoring the intricate thermal behavior of the studied materials. [6]. The amount of solid residue of B-MgFe-BC and MgFe-AC left after 800 °C was 34.7% and 29.31% respectively. The initial weight loss observed in biochar occurs at temperatures below 108 °C and is attributed to the evaporation of moisture content. The presence of moisture

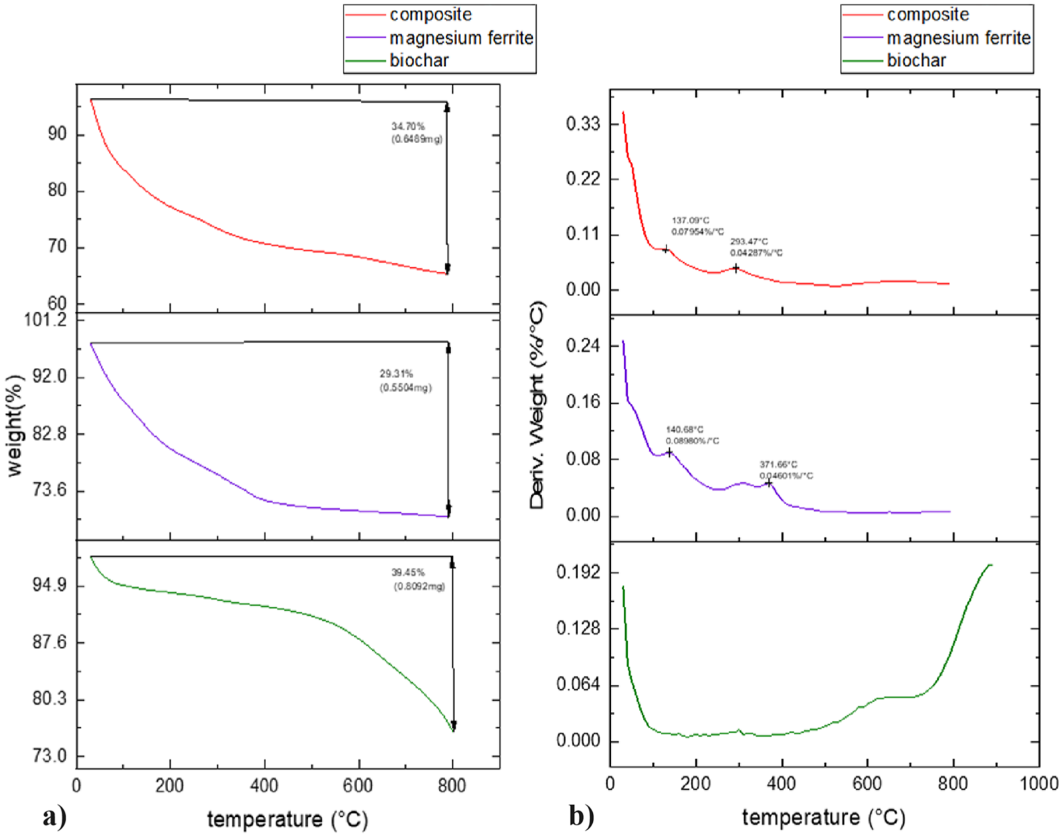

Fig. 5 a) Weight loss profiles and b) DTG for B-MgFe-BC, MgFe-AC and biochar

in the biochar samples is indicative of the material's hygroscopic nature. The subsequent substantial weight loss can be attributed to the expulsion of volatile components, leading to an increase in the proportion of fixed carbon in the biochar. This phenomenon is associated with the thermal breakdown of carbohydrates within the biochar at elevated temperatures during thermogravimetric analysis [4] The biochar showed an overall weight loss of 60.55% at 800 °C.

Thermogravimetric analysis (TGA) played a key role in understanding the interplay between the adsorbent's functional groups and its effectiveness at higher temperatures. These functional groups, like carboxyl groups (C=O) and hydroxyl groups (O-H), are crucial for capturing target pollutants through ion exchange and hydrogen bonding. By pinpointing the decomposition temperatures of these functionalities through TGA, we can anticipate potential limitations of the adsorbent. This knowledge is instrumental in optimizing operating conditions to ensure the adsorbent's optimal performance and longevity at elevated temperatures.

3.1.3 Study of surface morphology

The investigation into biochar, B-MgFe-BC, and MgFe-AC involved a thorough examination of their morphological traits as shown in Fig. 6. Upon close examination of the SEM image of biochar, it is discernible that the pyrolysis process has not only induced porous structures but has also contributed to their intricate development. The uniformity and integrity of these pores are notably enhanced due to the simultaneous pyrolysis of lignin in rice husks along with hemicellulose. Furthermore, the surface roughness observed can be attributed to the volatilization of water and the gradual decomposition of hemicellulose, providing additional insights into the material's structural evolution [32].

In contrast, the SEM image of MgFe-AC showcased distinct areas of agglomeration, a phenomenon arising from the inherent interaction among magnetic nanoparticles. This observation aligns with the common tendency of nanoparticles, particularly in nanocrystalline spinel ferrites, to exhibit a propensity for aggregation [11]. Examining the SEM image of B-MgFe-BC, a unique feature becomes evident—the agglomerated MgFe-BC particles are intricately attached to the surface of biochar. This distinctive configuration in the composite material underscores the interplay between MgFe-BC and biochar, contributing to the overall morphology of B-MgFe-BC. Although B-MgFe-BC contains MgFe agglomerates, their size is demonstrably smaller compared to those found in MgFe-AC. This significant disparity in size plays a crucial role in explaining the higher surface area observed in B-MgFe-BC. Smaller

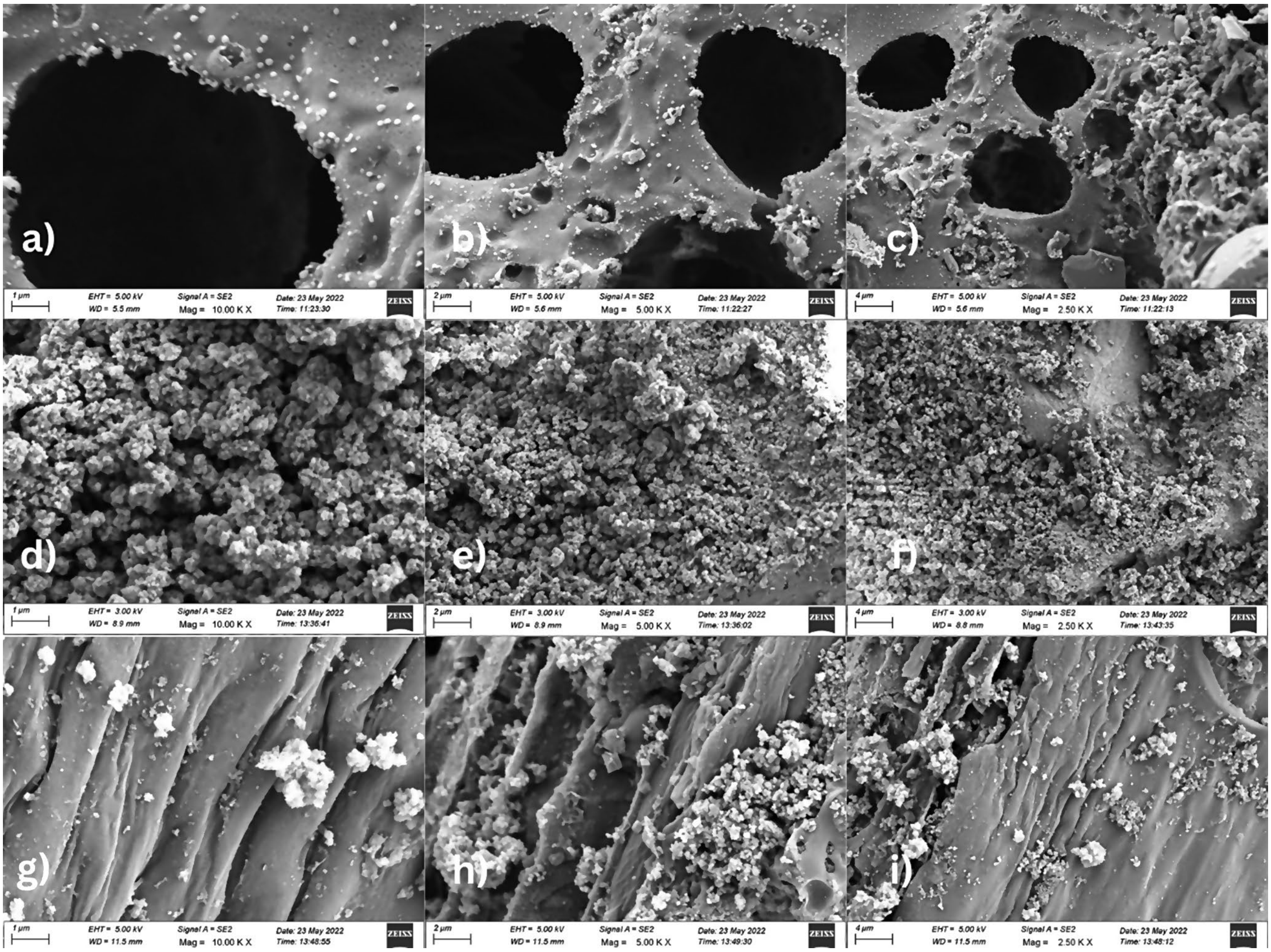

Fig. 6 SEM images of (**a**-**c**) biochar (**d**-**f**) MgFe-AC (**g**-**i**) B-MgFe-BC

agglomerates create a more dispersed network within the material, maximizing the available surface area for interaction. In contrast, larger agglomerates in MgFe-AC likely pack more densely, resulting in a reduced overall surface area accessible for adsorption.

Examination by scanning electron microscopy (SEM) revealed the morphological and microstructural characteristics of the various adsorbents. These observations likely contribute to the superior performance of B-MgFe-AC in removing chromium and nickel ions.

3.1.4 Surface analysis

The N_2 adsorption analysis highlights a significant BET surface area of 151.319 m²/g for B-MgFe-BC. Additionally, Barrett–Joyner–Halenda (BJH) analysis of pore characteristics indicates an average pore diameter of 1.5365 nm and a total pore volume of 0.17 cm³/g. These findings affirm the microporous nature of B-MgFe-BC, characterized by pores with sizes less than 2 nm.

Similarly, the N_2 adsorption analysis reveals a substantial BET surface area of 91.375 m²/g for MgFe-AC. BJH analysis of pore characteristics indicates an average pore diameter of 1.54 nm and a total pore volume of 0.37 cm³/g. These results also establish MgFe-AC's microporous structure, featuring pores with sizes less than 2 nm.

Adsorption isotherm models, by taking into consideration both the equilibrium data and the adsorption properties, describe the interaction mechanisms of pollutants and adsorbent materials. It is evident from Fig. 7(a) and Fig. 7(b) that the isotherm for B-MgFe-BC and MgFe-AC can be classified as Type II. When dealing with the adsorption isotherm of Type II, determining a suitable model involves recognizing specific curve characteristics. In this scenario, the curve signifies multi-anchorage adsorption and displays negative concavity, indicating that the parameter "n" is less than unity at low concentrations. Additionally, at higher concentrations, there is a noticeable divergence in the adsorbed quantity, suggestive of a condensation phenomenon. Consequently, the nature of this behavior aligns with a

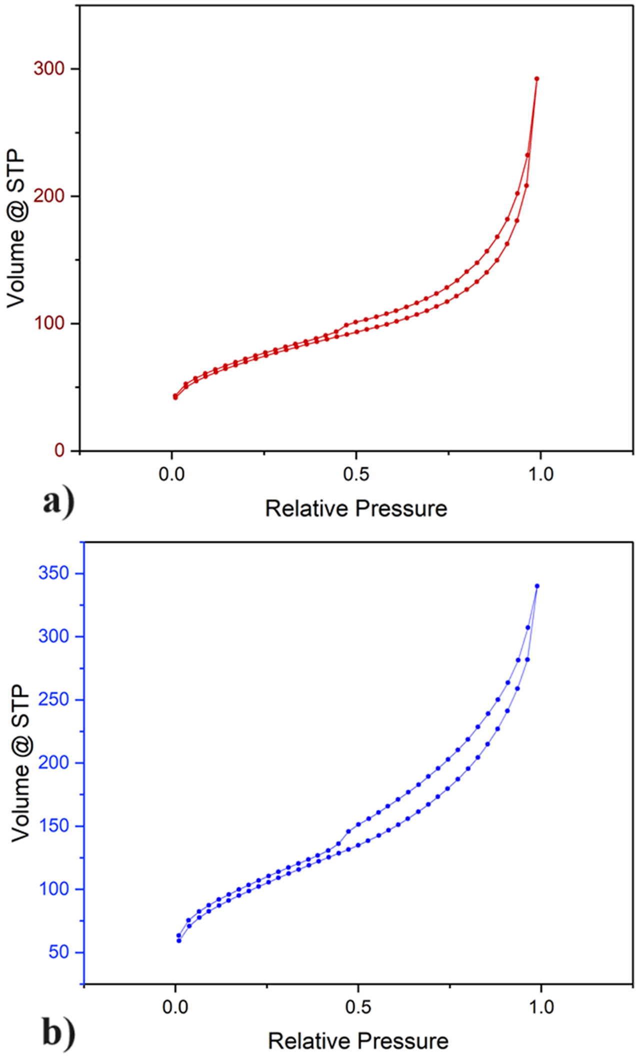

Fig. 7 BET Isotherm plot for Nitrogen adsorption capacity of (**a**) B-MgFe-BC and (**b**) MgFe

multilayer model, as the occupation number encompasses a continuum from zero to infinity, signifying the potential for multiple adsorption layers [16].

The Type II isotherm characterizes the adsorption behavior on mesoporous monolayer materials at low pressure and on mesoporous multilayer materials at high pressure, particularly approaching saturation, without displaying hysteresis. It exhibits a single inflection point and is observed exclusively in microporous, nonporous, or dispersed solids with pore diameters exceeding 50 nm [1].

3.1.5 Particle size analysis

The results of the particle size analysis reveal distinctive characteristics among biochar, the B-MgFe-BC, and MgFe-AC as shown in Fig. 8(a), (b) and (c) respectively. The Z average for biochar is measured at approximately 172 nm, while B-MgFe-BC exhibits a significantly larger particle size with a Z average of 355 nm. In contrast, MgFe-AC showcases a comparatively larger Z average of 500 nm. This indicates that the particle size of biochar is smaller than that of both MgFe-AC and B-MgFe-BC. Notably, the MgFe-AC stands out with the highest Z average, signifying a larger average particle size compared to the other materials. These findings are crucial for understanding the size distribution of particles in each material, offering insights into their potential applications and properties in various fields.

3.2 Batch adsorption experiments

3.2.1 pH influence on nickel and chromium adsorption

To investigate the impact of pH on the adsorption of nickel and chromium by B-MgFe-BC, we examined the adsorption capacity and efficiency under varying pH conditions in the solution. The addition of 0.6 gm of B-MgFe-BC to the solution was kept constant while maintaining a temperature of 60 °C and a contact time of 120 min. The initial concentration of nickel or chromium ions in the solution was 50 ppm.

As illustrated in Fig. 9, the uptake of nickel ions exhibited a noticeable trend with changing pH values in the aqueous solution. It increased from 90% at pH 1 to 96.6% at pH 6, and then slightly decreased to 96.4% as the pH further increased to 8. Concurrently, the amount of nickel ions removed per gram of B-MgFe-BC demonstrated a similar pattern, rising from 3.75 mg/g at pH 1 to 4.01 mg/g at pH 6, and then decreasing marginally to 4.025 mg/g.

This observed behavior can be elucidated by considering the chemical interactions between the ions in the aqueous solution and the functional groups present on the adsorbent's surface. At lower pH levels, there is a competition between hydrogen ions and nickel metal ions for the active adsorption sites. As the pH increases, the adsorption surface becomes less positively charged, thereby enhancing the electrostatic attraction between the metal ions and the B-MgFe-BC surface. The peak adsorption efficiency around neutral pH suggests a significant interaction of Ni^{2+}, $Ni (OH)^+$, and $Ni (OH)_2$ with the functional groups on the adsorbent's surface. A slight decline in adsorption at higher pH values is attributed to the formation of soluble hydroxyl complexes. These species undergo adsorption on the B-MgFe-BC surface through an ion exchange mechanism or by forming hydrogen bonding with the functional groups, explaining the nuanced pH-dependent adsorption behavior [23].

As depicted in Fig. 9, the adsorption of chromium ions displayed a discernible pattern as pH values in the aqueous solution varied. It declined from 97% at pH 1 to 88.6% at pH 8. Simultaneously, the quantity of chromium ions removed per gram of B-MgFe-BC exhibited a comparable

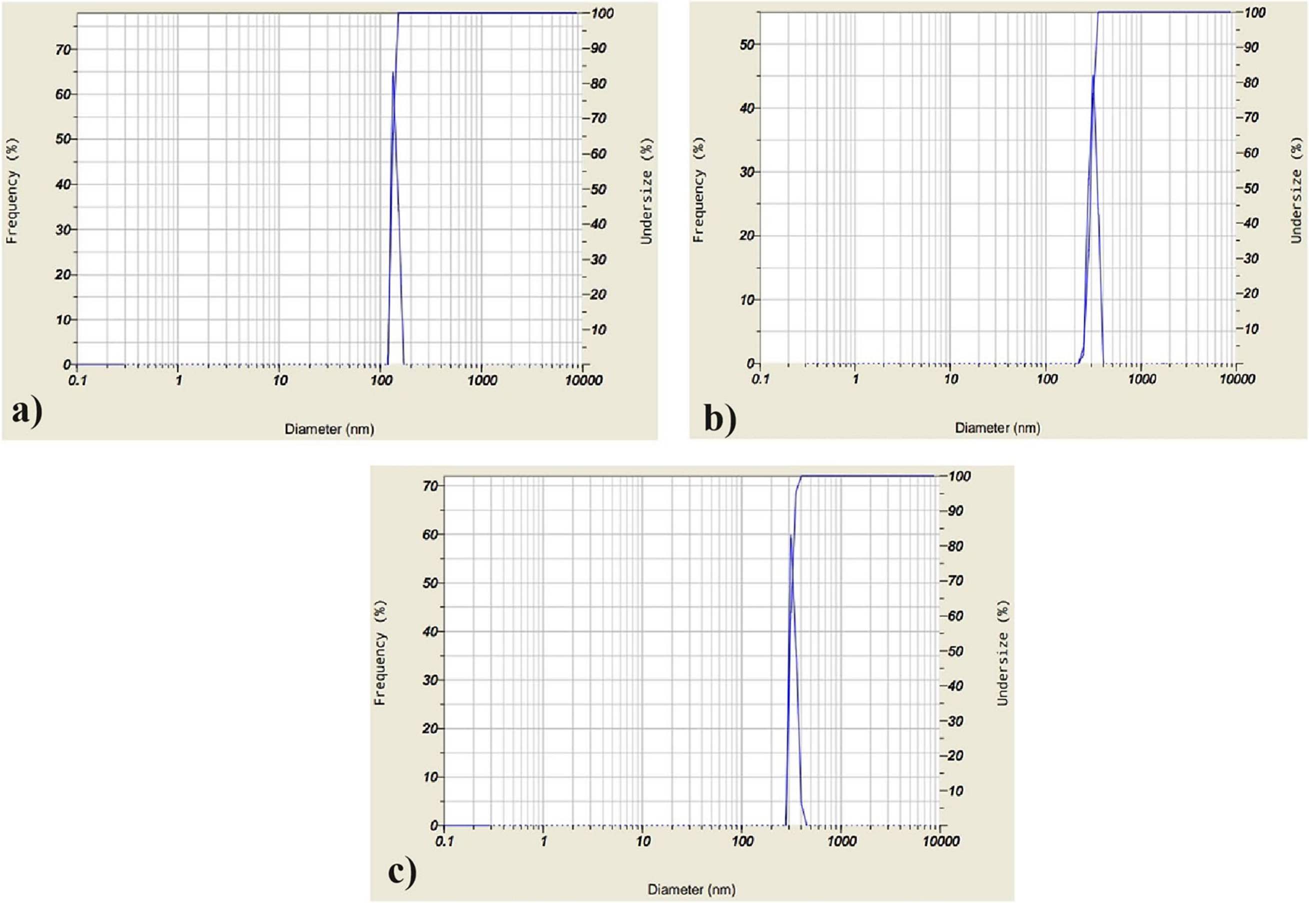

Fig. 8 Particle size analysis of (**a**) biochar (**b**) B-MgFe-BC (**c**) MgFe-AC

trend, decreasing from 4.04 mg/g at pH 1 to 3.69 mg/g at pH 8.

Hexavalent chromium exists in different chemical forms in aqueous solutions, including $HCrO_4^-$, $Cr_2O_7^{2-}$, and CrO_4^-. The stability of these forms is closely tied to the pH of the system. In acidic conditions, chromium ions primarily take on the form of Hydrogen Chromate ($HCrO_4^-$), a negatively charged species that forms bonds with the positively charged surface of B-MgFe-BC. The removal efficiency is notably enhanced in acidic environments due to the robust oxidation and reduction reactions, leading to more effective elimination. Consequently, adsorption efficiency experiences a significant increase under acidic conditions. However, as the pH of the solution gradually increases, chromium undergoes a transformation towards CrO_4^{2-} and $Cr_2O_7^{2-}$. The heightened concentration of OH^- ions leads to increased competitive adsorption between OH^- and these negatively charged species, inhibiting their adsorption. Consequently, under acidic conditions, the adsorption efficiency surpasses that observed under alkaline conditions. The decrease in efficiency can also be attributed to the fact that, as pH increases, the adsorption surface becomes less positively charged, diminishing the electrostatic attraction between the negatively charged species and the B-MgFe-BC surface [13].

To determine the ideal operating pH for B-MgFe-BC, we measured its point of zero charge (pHpzc). This is the pH at which the adsorbent surface has no net electrical charge. The experiment involved treating B-MgFe-BC with a salt solution (NaCl) at various pH levels (between 1 and 8) achieved using acid (0.1 M HCl) and base (0.1 M NaOH). After shaking the mixtures for 24 h, the change in pH (ΔpH) was measured. Plotting this ΔpH against the initial pH revealed the pHpzc at the point where the curve crosses the x-axis. In this case, the pHpzc was estimated to be 4.1 (as shown in Fig. 10). This value is crucial because it determines the surface charge of B-MgFe-BC. When the solution pH is lower than the pHpzc ($pH < 4.1$), the adsorbent surface becomes positively charged. This positive charge is favorable for attracting and adsorbing negatively charged chromate ions at lower pH values. However, it has the opposite effect on positively charged nickel ions, as electrostatic repulsion hinders their adsorption.

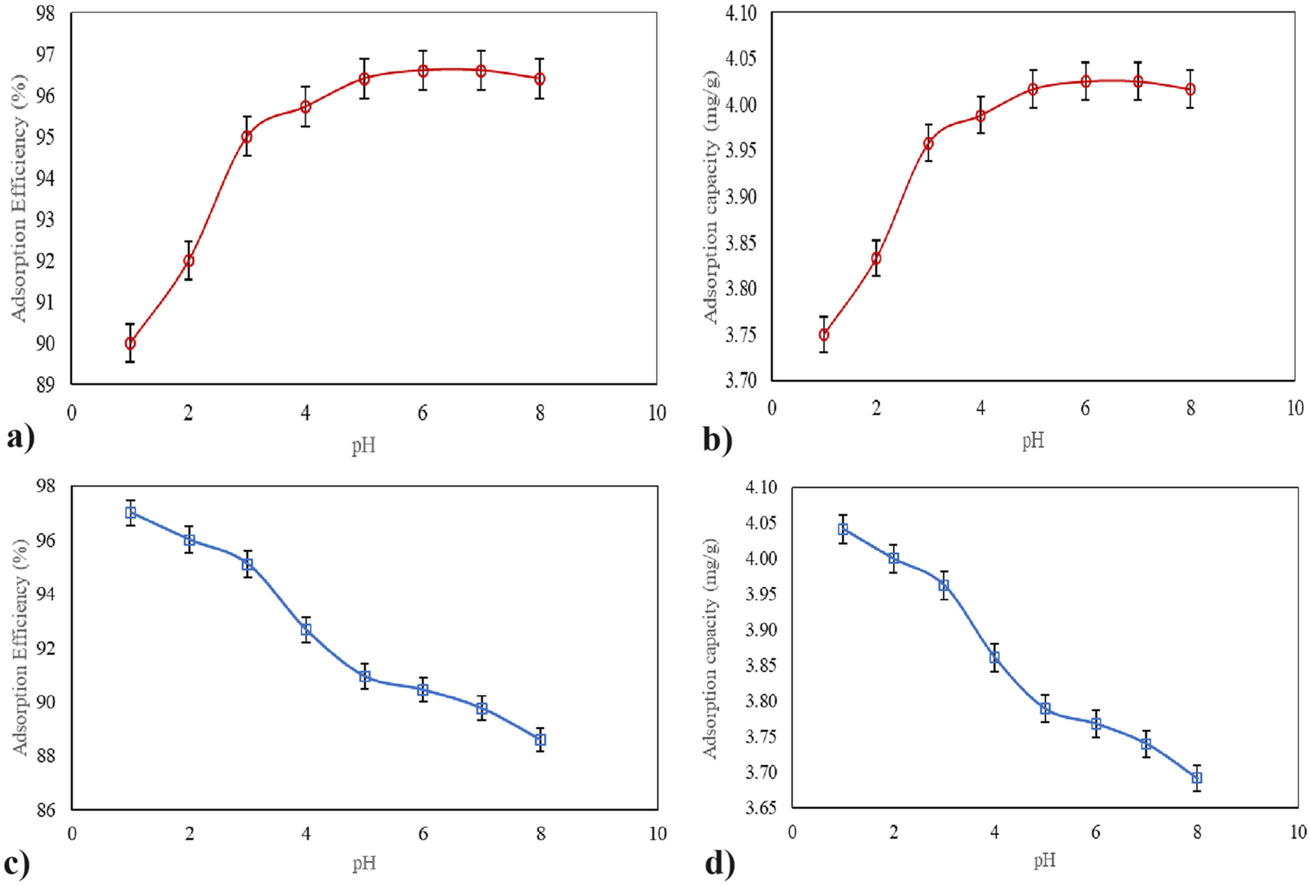

Fig. 9 Influence of pH on the adsorption of (**a**)-(**b**) nickel and (**c**)-(**d**) chromium ions

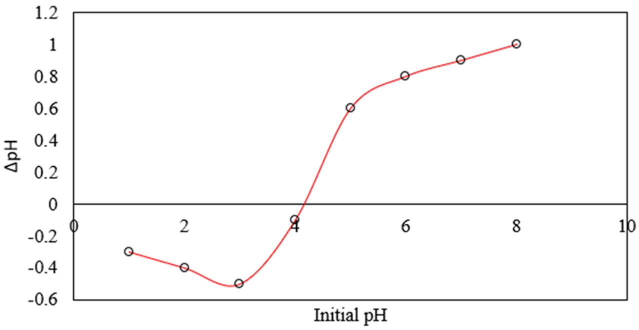

Fig. 10 Determination of the pH of zero point of charge (pHZPC)

3.2.2 Influence of initial chromium and nickel Ion concentrations and isothermal modeling

The adsorption properties of B-MgFe-BC (a blend of biochar and magnesium ferrite before calcination) are notably affected by the concentration of nickel and chromium ions present in the aqueous state. The investigation involved manipulating initial concentrations, specifically at 50, 100, 200, 300, 400 and 500 ppm of nickel and chromium ions. The testing was conducted at a temperature of 60 °C, incorporating 0.6 gm of B-MgFe-BC into the solution, and ensuring a consistent contact time of 120 min.

As portrayed in Fig. 11, it is clear that the efficacy of the B-MgFe-BC in removing nickel ions experiences a marginal rise, moving from 99.36 to 99.79% as the concentration at the outset elevates from 50 ppm to 200 ppm. Subsequently, a sharp decline in the removal rate is observed, reaching 92.87% at an initial concentration of 500 ppm, which is still considered satisfactory. Contrarily, the adsorption capability displayed an almost linear advancement, initiating at 4.14 mg/g with a starting concentration of 50 ppm nickel ions, and peaking at 38.69 mg/g with an initial concentration of 500 ppm nickel ions.

As depicted in Fig. 11, an analogous trend is evident when examining variations in the concentration of chromium ions in the solution at the outset. The marginal uptick in adsorption efficiency, moving from 99.3 to 99.8%, corresponds to an increase in the initial concentration from 50 ppm to 200 ppm. Following this, a pronounced decrease in the removal rate is noted, reaching 92.9% at an initial concentration of 500 ppm, which remains within acceptable limits. Conversely, the adsorption capacity demonstrates an almost linear advancement. It initiates at 4.13 mg/g with a

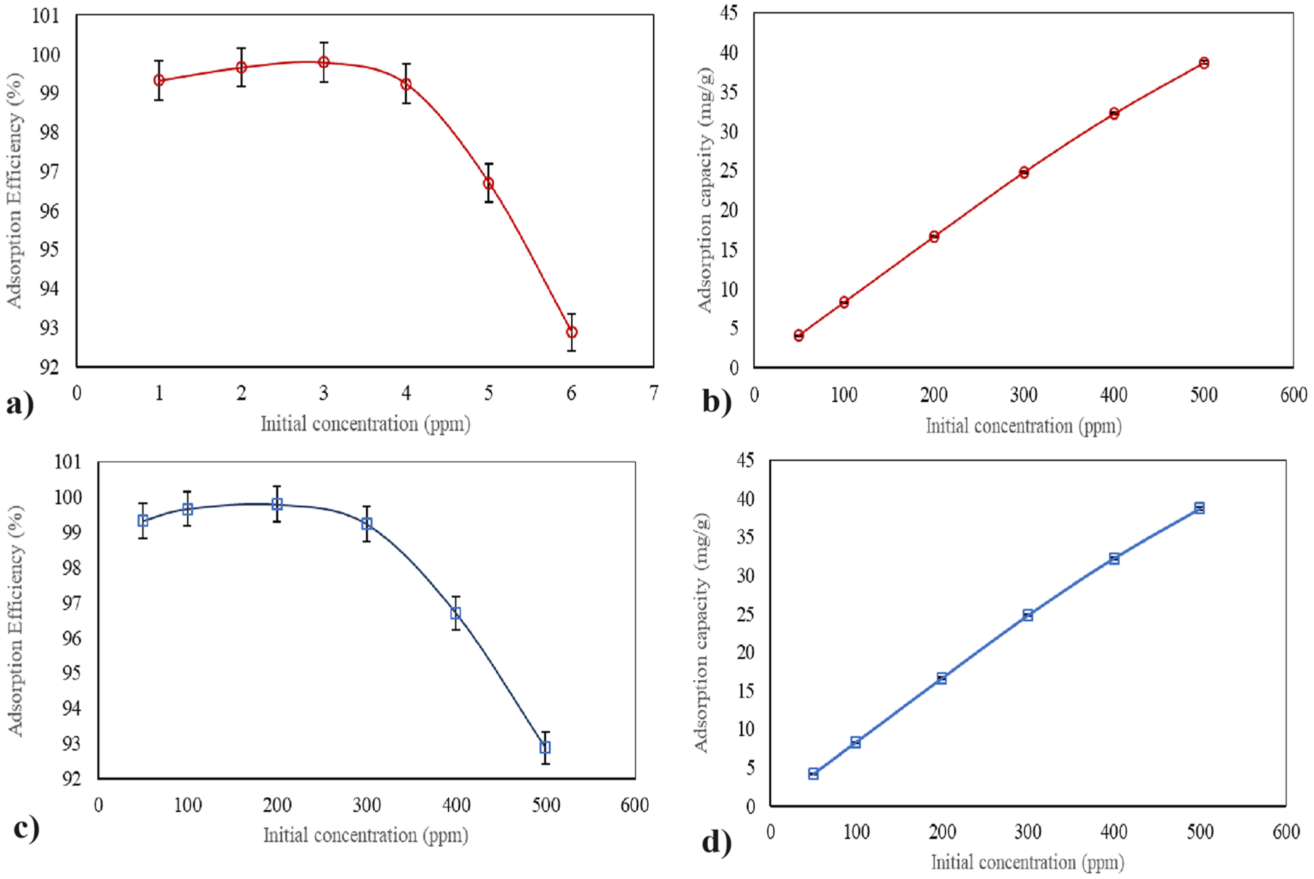

Fig. 11 Influence of initial concentration on the adsorption of (**a**)-(**b**) nickel and (**c**)-(**d**) chromium ions

50-ppm initial concentration of chromium ions and peaks at 38.69 mg/g with an initial concentration of chromium ions at 500 ppm.

These findings underscore the dependence of the adsorption process on the initial concentration of chromium or nickel in the solution. Moreover, it is evident that adsorption efficiency diminishes, with an increase in the concentration of nickel and chromium at the outset. This phenomenon occurs due to the surplus of functional groups and active adsorption sites on the surface of B-MgFe-BC when the amount of chromium and nickel at the outset is low. Consequently, B-MgFe-BC exhibits heightened adsorption efficiency, rapidly adsorbing a substantial quantity of metal ions. The decline in the removal percentage at elevated concentrations could be ascribed to the saturation of adsorption sites on the adsorbents. The proportion of the accessible surface to the initial concentration of metal ions decreases. This saturation, consequently, results in a greater number of chromium or nickel ions remaining unadsorbed in the aqueous state, owing to heightened competition among ions for the limited binding sites available. (Bansal et al., 2009).

The heightened adsorption capacity can be ascribed to an increased rate of mass transfer driven by a higher concentration gradient. When the amount of nickel and chromium ions at the outset is modest, external surface adsorption points are initially occupied. However, with a rise in concentration, the B-MgFe-BC's concentration gradient amplifies, facilitating the migration of metal ions to the internal channels for removal. This utilization of additional adsorption sites corresponds to an increased adsorbent quantity in tandem with the heightened initial concentration (Yang et al., 2018).

An isotherm illustrates the connection that the concentrations of heavy metal ions at equilibrium in the aqueous solution have with the corresponding adsorption capacity on the surface of B-MgFe-BC at a specific temperature. Its characteristics are contingent upon factors such as the heavy metal ions adsorbed, the nature of nickel and chromium and B-MgFe-BC, and the physical properties of the aqueous state, encompassing pH, ion concentration, and temperature [28]. To glean an understanding of the adsorption mechanism involving heavy metal ions and B-MgFe-BC, we applied the Langmuir, Freundlich, Temkin and Dubinin-Radushkevich isotherm equations (S1, S2, S3, and S4 respectively) to fit the equilibrium adsorption data of heavy metal ions.

The isotherm plots for nickel and chromium are available in Fig. 12(a) and (b) respectively.

The isotherm constants for nickel and chromium adsorption are given in Table 1.

It is evident that Temkin Isotherm showed a better fit for the adsorption of nickel as well as chromium ions. According to this isotherm, the heat of adsorption is expected to exhibit a linear decrease, accompanied by a uniform distribution of binding energies, until reaching a maximum binding energy. The Temkin isotherm values suggest that the adsorption process took place through physisorption. The bonding energy, which was less than 8 kJ mol^{-1}, further supports the conclusion that the mechanism involved in adsorption is physical in nature. In physisorption, the adsorbates attach to the adsorbent through weak van der Waals interactions, leading to relatively low adsorption energies in this process [5]. The monolayer adsorption capacity was found to be 54.05 mg/g for nickel adsorption and 50.00 mg/g for chromium adsorption. Additionally, the mean free energy of adsorption from the Dubinin-Radushkevich (D-R) plot for both nickel and chromium adsorption is less than 8 kJ/mol, another indicator of a physical adsorption mechanism. Analysis of the Freundlich isotherm reveals a parameter value (n) between 0 and 10, suggesting favorable adsorption conditions. These results suggest that the material has a high affinity for both nickel and chromium ions. The adsorption capacity values are comparable, indicating that the material can effectively adsorb similar amounts of both metals.

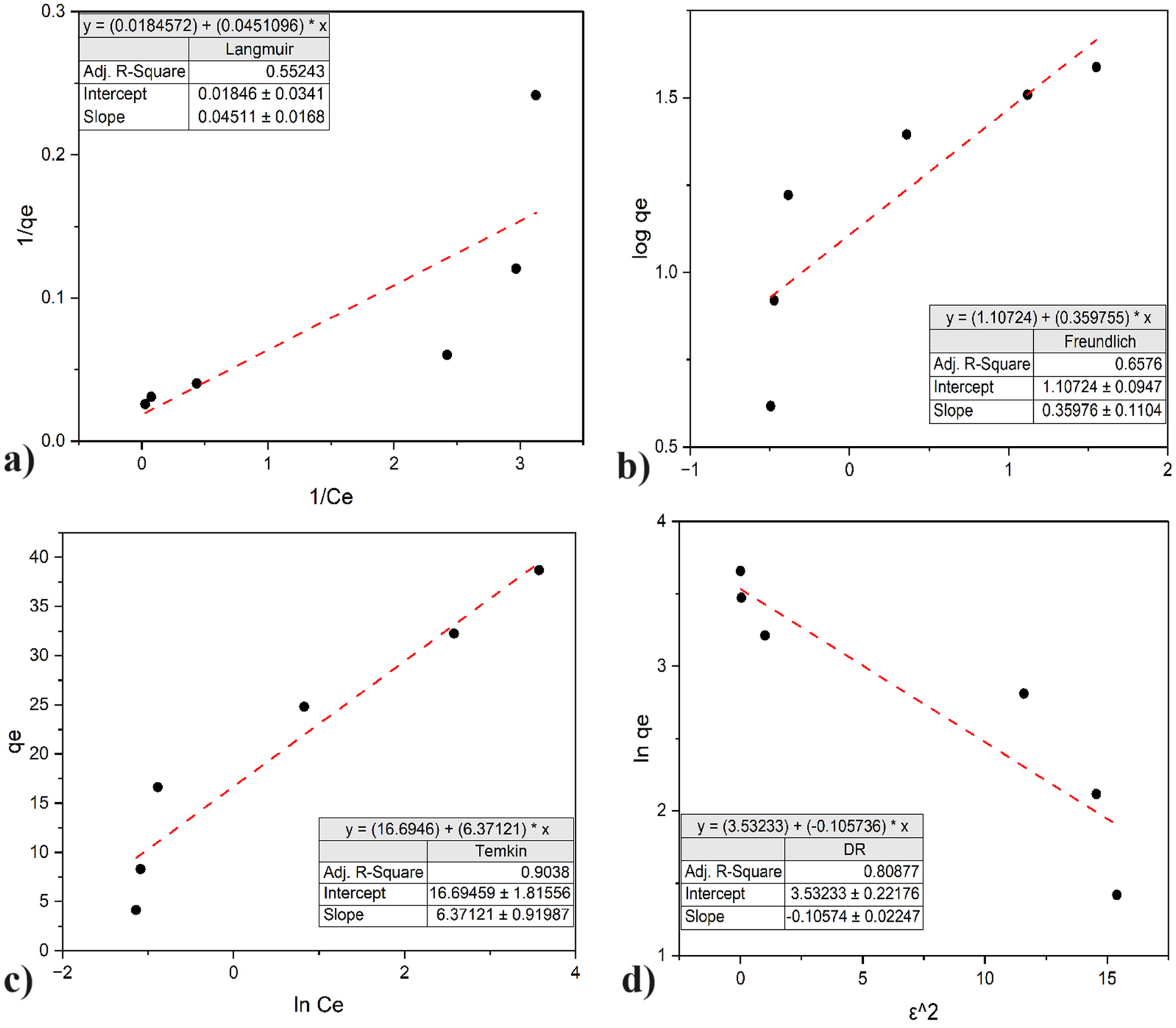

y = (0.0184572) + (0.0451096) * x

	Langmuir
Adj. R-Square	0.55243
Intercept	0.01846 ± 0.0341
Slope	0.04511 ± 0.0168

y = (1.10724) + (0.359755) * x

	Freundlich
Adj. R-Square	0.6576
Intercept	1.10724 ± 0.0947
Slope	0.35976 ± 0.1104

y = (16.6946) + (6.37121) * x

	Temkin
Adj. R-Square	0.9038
Intercept	16.69459 ± 1.81556
Slope	6.37121 ± 0.91987

y = (3.53233) + (-0.105736) * x

	DR
Adj. R-Square	0.80877
Intercept	3.53233 ± 0.22176
Slope	-0.10574 ± 0.02247

Fig. 12 **A**) a) Langmuir b) Freundlich c)Temkin and d) Dubinin-Radushkevich Isotherm plots for nickel ion adsorption

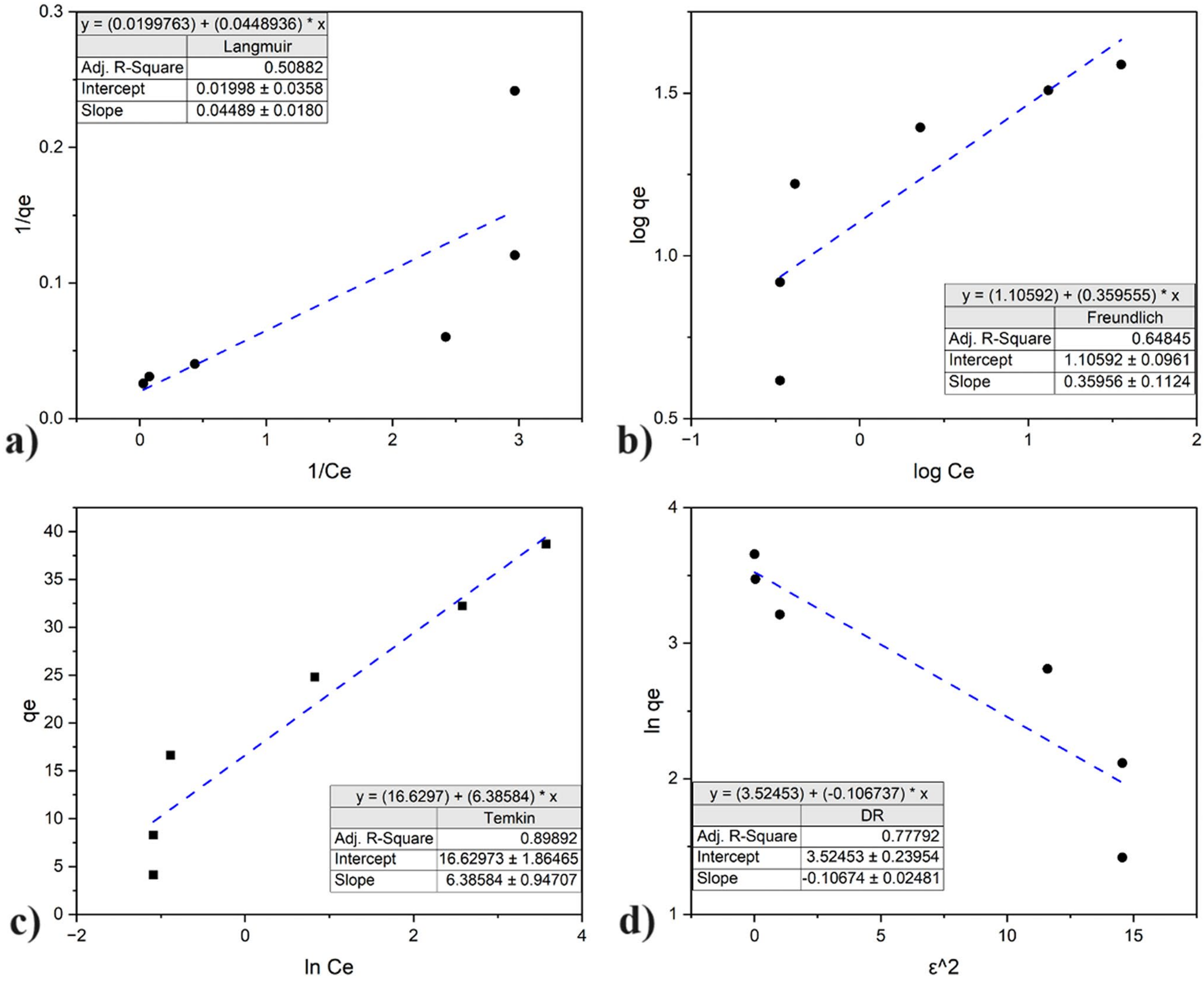

Fig. 12 **B**) a) Langmuir b) Freundlich c)Temkin and d) Dubinin-Radushkevich Isotherm plots for chromium ion adsorption

Table 1 Isotherm constants for various models

Langmuir isotherm:	nickel	chromium
	Q_{max} = 54.05 mg/g K_L = 0.41 L/mg	Q_{max} = 50.00 mg/g K_L = 0.44 L/mg
Freundlich Isotherm:	$n = 2.77$ K_f = 12.79 (mg/g)(L/mg)$^{1/n}$	$n = 2.49$ K_f = 11.21 (mg/g)(L/mg)$^{1/n}$
Temkin	B = 6.37 K_T = 13.74 L/g b_T = 0.43 J/mol	B = 6.37 K_T = 7.40 L/g b_T = 0.397 J/mol
Dubinin-Radushkevich	K = 0.11 mol^2 /kJ^2 q_m = 34.20 mg/g E = 2.17 kJ/mol	K = 0.11 mol^2 /kJ^2 q_m = 34.06 mg/g E = 2.16 kJ/mol

3.2.3 Effect of initial concentration in binary metal ion solution

The investigation delved into the simultaneous adsorption dynamics of chromium and nickel ions in binary mixtures, employing a range of initial concentrations for both elements in the solution. The findings, as depicted in the accompanying Fig. 13, unveil intriguing trends. Notably, as the initial concentrations of nickel and chromium ions elevate from 50 ppm to 500 ppm, the equilibrium uptake of nickel ions exhibits remarkable constancy. In contrast, the equilibrium removal of chromium experiences a notable and precipitous decline.

Upon closer examination, it becomes evident that the adsorption behavior of the B-MgFe-BC material is distinctly influenced by the interplay between nickel and chromium ions. The adsorption of nickel ions per gram of B-MgFe-BC and chromium ions both exhibit an upward trajectory with escalating initial concentrations. However, a nuanced observation reveals that the equilibrium removal percentage of chromium ions witnesses a substantial drop at higher concentrations. This decline is attributed to the saturation of

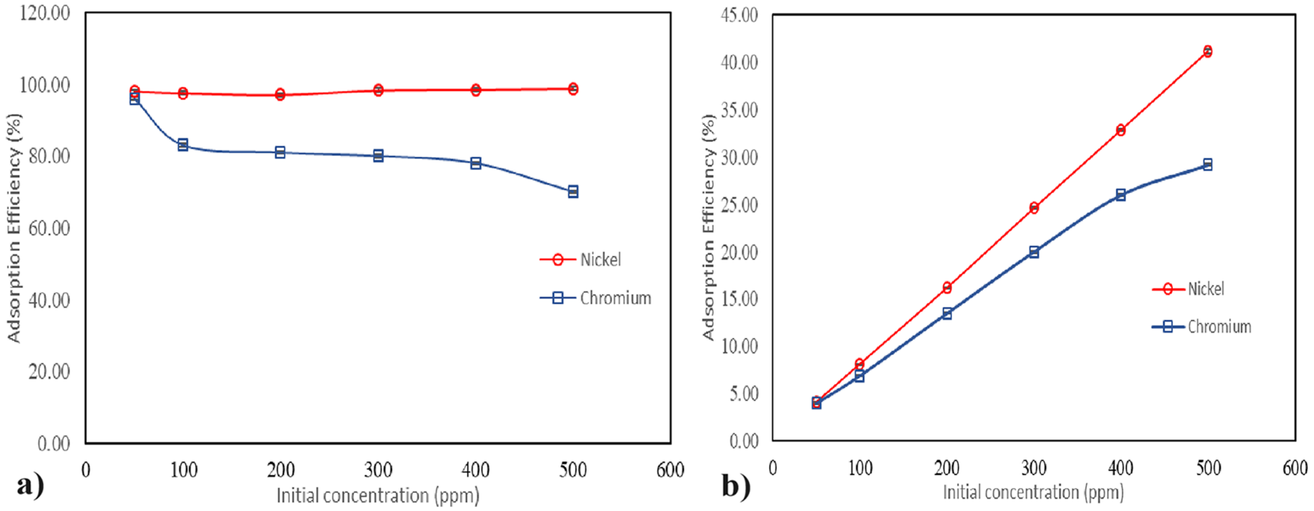

Fig. 13 Influence of initial concentration on (**a**) Adsorption Efficiency and (**b**) Adsorption Capacity

binding sites on B-MgFe-BC, primarily due to the intensified adsorption of nickel ions.

The heightened affinity of the adsorbent towards nickel ions is underscored by this phenomenon. The ratio of available surface area to the initial metal ion concentration diminishes as nickel ions saturate binding sites, leading to heightened competition among ions for the limited available spaces. Consequently, a greater number of chromium ions remain unadsorbed in the solution.

The increased adsorption capacity as shown in Fig. 13 is rationalized by an augmented rate of mass transfer, driven by a steeper concentration gradient. In scenarios where the initial concentration of heavy metal ions is modest, external surface adsorption points are preferentially occupied. However, as the concentration rises, the concentration gradient of B-MgFe-BC intensifies, facilitating the migration of metal ions into internal channels for removal. This utilization of additional adsorption sites corresponds to a proportional increase in the quantity of adsorbent, aligning with the heightened initial concentration. The intricate interplay between concentration dynamics, surface saturation, and competition for binding sites thus orchestrates the nuanced adsorption phenomena observed in this binary system.

3.2.4 Investigating the influence of contact time and kinetic studies

Optimal contact time is imperative for maximizing the efficiency of the adsorption process. The influence of contact time on adsorption dynamics was examined by varying the duration from 0 to 120 min at 10-minute intervals. The initial concentration of heavy metal ions remained at 50 ppm, while the temperature was held constant at 60 °C, and the adsorbent dosage was 0.6 g.

The B-MgFe-BC's effectiveness in removing nickel ions escalates with an extended contact time until equilibrium is achieved. Starting at a 10-minute contact time, the adsorption efficiency stood at 55%, ultimately reaching an equilibrium value of 70.5% after 100 min. The quantity of adsorbate adsorbed per gram of the B-MgFe-BC experienced a gradual increase, initiating at 2.29 mg/g at 10 min and stabilizing at 2.93 mg/g by the 120th minute as shown in Fig. 14.

A parallel trend was discerned in the interaction between the B-MgFe-BC and chromium. The B-MgFe-BC's capacity to remove chromium ions rises with prolonged contact time until reaching a saturation limit. At a 10-minute contact time, the adsorption efficiency reached 79%, culminating in an equilibrium value of 86.6% after 120 min. The adsorption capacity of B-MgFe-BC also exhibited a marginal increase, commencing at 3.29 mg/g at 10 min and stabilizing at 3.6 mg/g after 120 min as shown in Fig. 14.

The obtained results indicate that achieving adsorption equilibrium for both heavy metal ions takes no more than 100 min. This concise duration underscores the robust affinity of B-MgFe-BC for metal ions in aqueous solutions. The findings propose a conceptualization of the adsorption process in three distinct stages. Initially, there is a rapid removal of chromium and nickel ions, driven by an accentuated concentration gradient at the interface between the B-MgFe-BC and aqueous solution. This facilitates a vigorous interaction, expediting the movement of chromium from the solution to the surface of B-MgFe-BC. Concurrently, the profusion of adsorption sites on the adsorbent enables a swift increase in the adsorbed quantity of chromium and nickel ions. Transitioning into the secondary adsorption stage, the pool of available surface adsorption sites on the B-MgFe-BC gradually diminishes. This reduction results in a corresponding

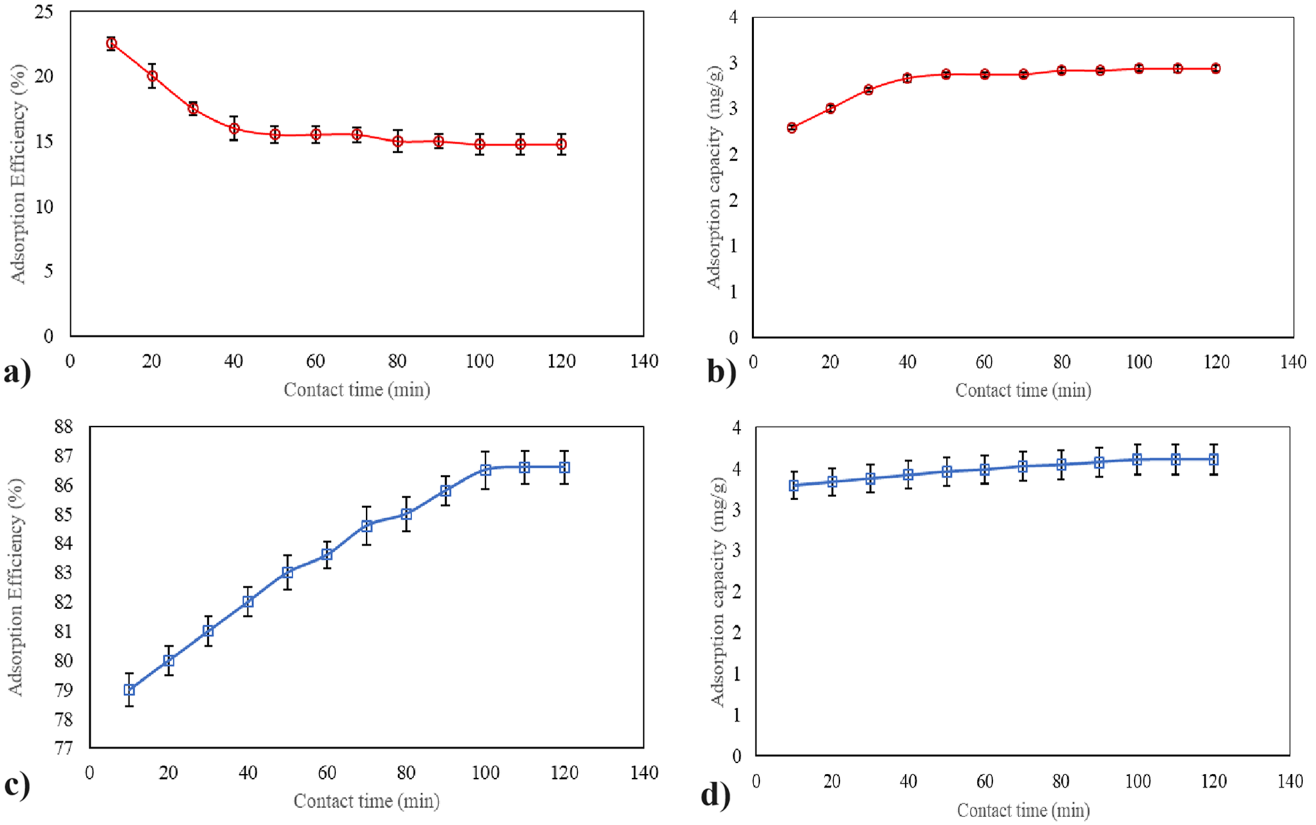

Fig. 14 Influence of contact time on adsorption of (**a**)-(**b**) nickel and (**c**)-(**d**) chromium ions

decline in the concentration gradient of nickel and chromium ions at the interface, mitigating repulsive interactions. Consequently, the adsorption rate decelerates, and the adsorption capacity for chromium and nickel ions experiences a more gradual upsurge. After 100 min in the process of adsorption, the reservoir of available sites of adsorption on the B-MgFe-BC approaches saturation. At this juncture, further attempts to enhance the adsorption capacity encounter challenges, and the system attains a state of adsorption equilibrium. [22].

Exploring the kinetics of adsorption offers valuable insights into the pace of adsorption, the efficacy of the selected adsorbent, and the underlying mechanisms governing mass transfer. This information plays a pivotal role in the formulation of efficient adsorption systems. The adsorption mass transfer kinetic process involves three primary stages. In the initial phase, external diffusion takes place as the nickel and chromium ions move through the liquid film surrounding B-MgFe-BC. External diffusion is driven by the concentration gradient between the bulk solution and the surface of B-MgFe-BC. Subsequently, the second stage encompasses internal diffusion, outlining the migration of the nickel and chromium ions within the pores of B-MgFe-BC. Finally, the third stage involves the adsorption of the ions onto the active sites of B-MgFe-BC. Diverse kinetic models, such as the Pseudo first-order and Pseudo second-order kinetic models, have been formulated to scrutinize and comprehend these intricate processes (S5 and S6) [27].

The linear plots for both nickel and chromium adsorption are depicted in Fig. 15.

The second-order kinetic model demonstrated a correlation coefficient close to unity, indicating the suitability of this model in describing the adsorption process. The first-order kinetic model assumes that the adsorption process occurs through a first-order reaction mechanism, where the rate of adsorption is directly proportional to the number of unoccupied sites on the adsorbent surface. In contrast, the pseudo-second-order model suggests that the rate of adsorption is influenced by the square of the number of adsorbate species on the surface, resulting in a non-linear relationship between adsorbate uptake and time. Additionally, the calculated q_e value of 3.02 mg/g, obtained from the pseudo-second-order kinetics, closely matched the experimental value of 4.14 mg/g for nickel adsorption. Similarly, the computed q_e value of 4.45 mg/g, derived from the pseudo-second-order kinetics, closely corresponded to the experimental value of 4.13 mg/g for chromium adsorption.

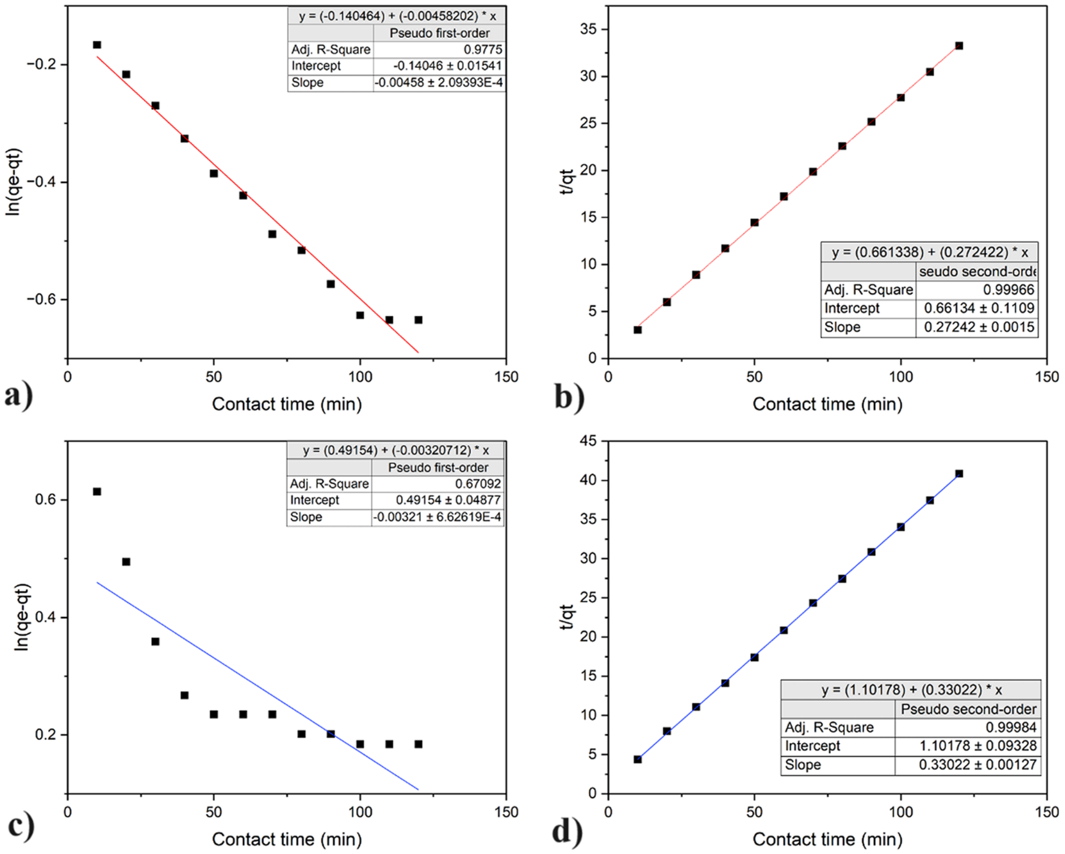

Fig. 15 Kinetic model of the adsorption of (**a**)-(**b**) nickel and (**c**)-(**d**) chromium ions

3.2.5 Investigating temperature influence and thermodynamic aspects

The solution temperature is a relevant operating parameter that affects the transport and kinetic processes of heavy metal ion adsorption. Hence the effect of temperature on adsorption was studied by varying the temperature to 30 °C,40 °C, 50 °C and 60 °C. The initial concentration of heavy metal ions remained at 50 ppm, while the adsorbent dosage was 0.6 g with a contact time of 120 min.

The ability of the adsorbent to effectively remove nickel ions increased from 64 to 98% when the temperature of the solution was raised. The adsorption capacity of the B-MgFe-BC also showed a similar trend having a value of 2.66 mg/g at 30 °C to 4.11 mg/g at 60 °C as shown in Fig. 16.

The efficacy of the adsorbent in efficiently eliminating chromium ions demonstrated a consistent pattern, escalating from 88.6 to 96.87% with an elevation in the solution temperature. Likewise, the adsorption capacity of B-MgFe-BC exhibited a parallel trend, registering a value of 3.69 mg/g at 30 °C and increasing to 4.03 mg/g at 60 °C as shown in Fig. 16.

Certainly, the observed rise in adsorption capacity with an increase in temperature is a consequence of the endothermic nature of the adsorption process, steering the adsorption equilibrium towards stronger adsorption [15]. This augmentation in adsorption capacity is intricately linked to the non-uniformity of the adsorbent, indicative of variations in the active energy of adsorption sites. At lower temperatures, sites with lower active energy are initially preferred, and as the temperature climbs, sites with higher active energy become increasingly occupied.

The heightened adsorption capacity at elevated temperatures can be explained by two key factors. Firstly, the increased kinetic energy of the B-MgFe-BC results in more frequent collisions between the B-MgFe-BC and heavy metal ions, thereby enhancing the adsorption process onto the absorbent's surface. Secondly, elevated temperatures induce greater breakage in bonds of functional groups at the adsorbent's surface, amplifying the accessibility of active adsorption sites. This substantiates an overall improvement in adsorption.

Hence, the temperature elevation exerts a beneficial influence by modulating the energy states of adsorption sites and augmenting the kinetic interactions of the B-MgFe-BC with heavy metal ions. The non-uniformity of the adsorbent plays a crucial role in this phenomenon, with temperature

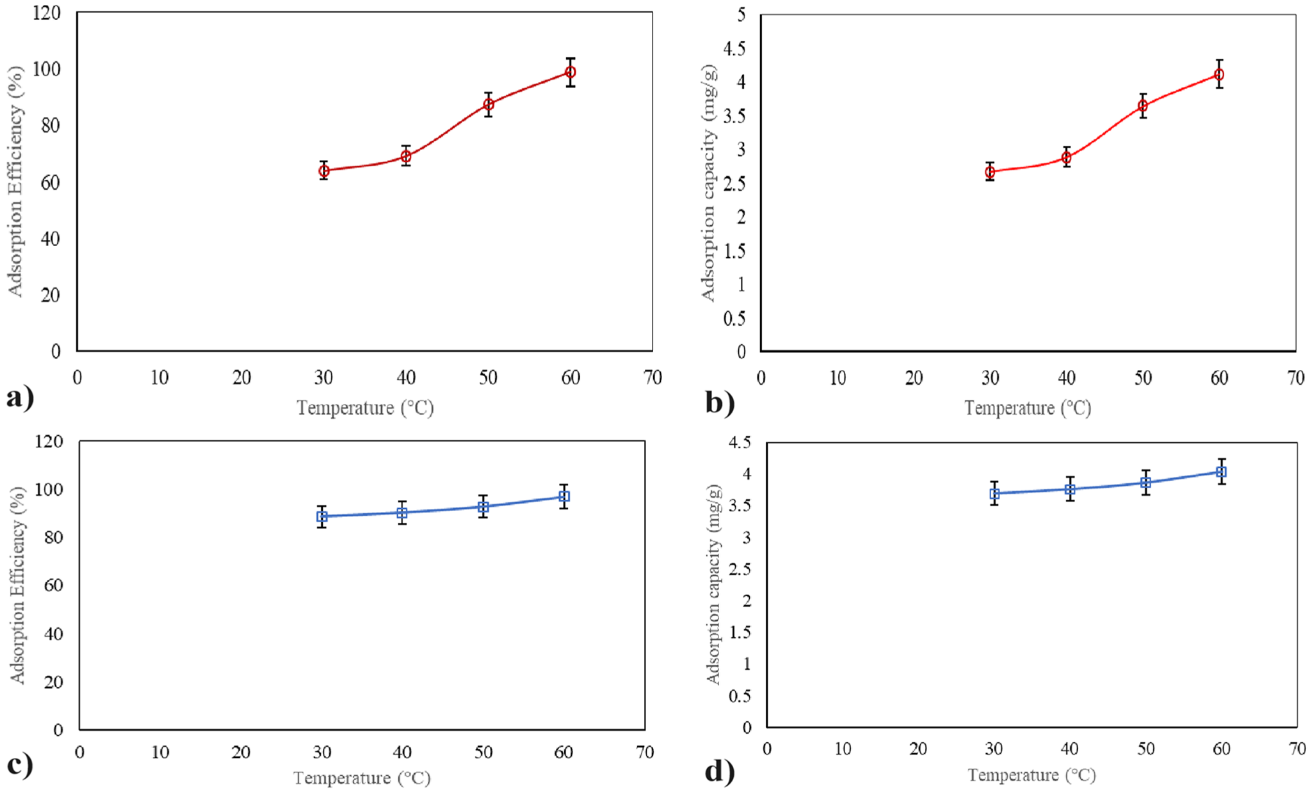

Fig. 16 Influence of Temperature on the adsorption of (**a**)-(**b**) nickel and (**c**)-(**d**) chromium ions

acting as a catalyst in optimizing the occupation of adsorption sites with varying active energies [28].

Determining thermodynamic parameters is crucial for understanding the energetics of an adsorption process. These parameters, including changes in Gibbs' free energy (ΔG°), enthalpy (ΔH°), and entropy (ΔS°), provide insights into whether the adsorption is feasible and shed light on its nature, whether it involves heat absorption (endothermic) or release (exothermic).

The process of calculating these thermodynamic parameters involves applying specific equations to experimental data. The Gibbs' free energy change is a key indicator of spontaneity, with negative values suggesting a spontaneous process. The enthalpy change reveals information about the heat exchange during adsorption, indicating whether it is an exothermic or endothermic reaction. Lastly, the entropy change reflects the disorder or randomness associated with the adsorption process.

The determination of these thermodynamic parameters from the experimental data was carried out utilizing the following equations:

$$\ln K_c = \frac{\Delta S^\circ}{R} - \frac{\Delta H^\circ}{RT}$$

$$\Delta G^\circ = -RT\ln K_c$$

$$\Delta G^\circ = \Delta H^\circ - T\Delta S^\circ$$

The equilibrium constant K_c can be obtained, and the values for the standard enthalpy change $\Delta H\circ$ in kilojoules per mole (kJ/mol) were obtained from the slope while the standard entropy change $\Delta S\circ$ in kilojoules per mole per Kelvin (kJ/mol K) was obtained from the intercept of the plot of the natural logarithm of K_c against the reciprocal of temperature as shown in Fig. 17 [17].

The thermodynamic parameters for nickel and chromium adsorption are given below in Table 2,

In the adsorption of both nickel and chromium ions by the adsorbent, a positive change in enthalpy was observed. This implies that the adsorption process is endothermic, explaining the heightened adsorption capacity and efficiency with an increase in temperature. The negative sign of the Gibbs free energy values further indicates that the adsorption is both feasible and spontaneous. Additionally, the positive value of the entropy change suggests an increased level of randomness in the adsorption process.

3.2.6 Regeneration and reusability

Desorption studies were conducted to check the reusability of B-MgFe-BC. It is evident from batch studies that B-MgFe-BC demonstrates maximum adsorption of nickel

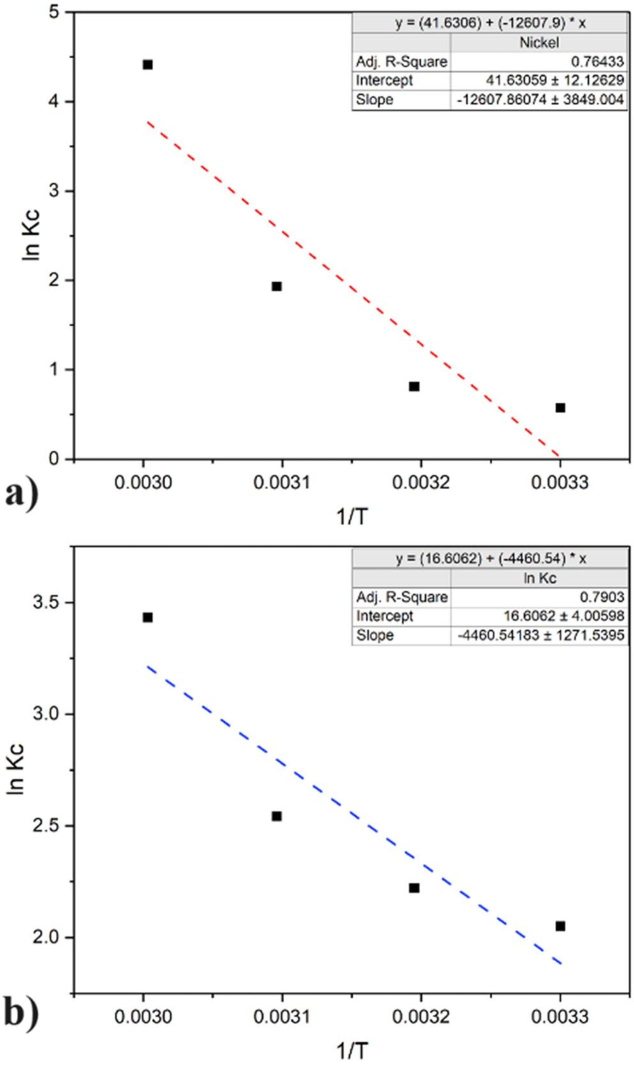

Fig. 17 Van't Hoff plot of the adsorption of (**a**) nickel and (**b**) chromium ions

Table 2 Thermodynamic parameters

		nickel	chromium
ΔH°		105.42 kJ / mol	37.08 kJ/mol
ΔS°		0.14 kJ / mol. K	0.35 kJ / mol. K
ΔG°	303 K	-1.45 kJ/mol	-5.17 kJ/mol
	313 K	-2.11 kJ/mol	-5.78 kJ/mol
	323 K	-5.19 kJ/mol	-6.83 kJ/mol
	333 K	-12.23 kJ/mol	-9.50 kJ/mol

ions under alkaline conditions while it shows maximum removal of chromium ions under acidic conditions. For this reason, NaOH was employed to study the desorption after the adsorption of chromium ions onto the surface of B-MgFe-BC while HCl was used to study the desorption after the adsorption of nickel ions.

The observed Fig. 18 demonstrates a direct correlation between the concentration of HCl and the desorption efficiency, showcasing an increase from 78 to 82%. This rise can be attributed to the displacement of nickel ions by H^+ ions derived from sulfuric acid. The rationale behind this lies in the higher electronegativity of H^+ ions compared to nickel ions. Essentially, this suggests that the adsorption of nickel by B-MgFe-BC is driven by electrostatic interactions, where the more electronegative H + ions replace nickel ions during the desorption process [10].

It is evident from Fig. 18 that with an increase in concentration of NaOH, the desorption efficiency also increases from 87 to 90%. As the pH of the solution gradually increases, chromium undergoes a transformation towards CrO_4^{2-} and $Cr_2O_7^{2-}$. The heightened concentration of OH^- ions leads to increased competitive adsorption between OH^- and these negatively charged species at the active sites of adsorption.

3.2.7 Mechanism of adsorption

B-MgFe-BC exhibits an adsorption mechanism for chromium ions analogous to the lock-and-key principle. Under acidic conditions, chromium primarily exists as negatively charged hydrogen chromate ($HCrO_4^-$), facilitating electrostatic interactions with the positively charged surface of B-MgFe-BC. At lower pH values, the abundance of hydrogen ions (H+) on the B-MgFe-BC surface promotes site-specific binding between the biomass functional groups and chromate anions. These chromate ions preferentially bind to active sites within the gelatin component due to their optimal size and compatibility. The encapsulation process is further enhanced by the smaller size of Cr(VI), leading to the effective capture of hexavalent chromium. Once encapsulated within the B-MgFe-BC matrix, these chromium ions migrate toward the core, where they interact with the iron centers. This interaction facilitates the reduction of hexavalent chromium (Cr(VI)) to trivalent chromium (Cr(III)). Due to its larger size, Cr(III) exhibits a weaker affinity for the active sites within the gelatin compared to Cr(VI). This weakened interaction allows Cr(III) to be desorbed from the B-MgFe-BC upon encountering hydroxide anions (OH-), forming chromium hydroxide (Cr(OH)3) which is subsequently washed away. This process effectively removes chromium ions from the surrounding solution [2].

At lower pH values, competition ensues between hydrogen ions (H+) and nickel cations (Ni^{2+}) for the coveted adsorption sites on B-MgFe-BC. This competition arises due to the positively charged nature of both the surface and H + ions. As the pH increases, the surface becomes progressively less positively charged. This creates a more favorable environment for electrostatic attraction between the negatively charged B-MgFe-BC surface and the positively charged nickel ions (Ni^{2+}).

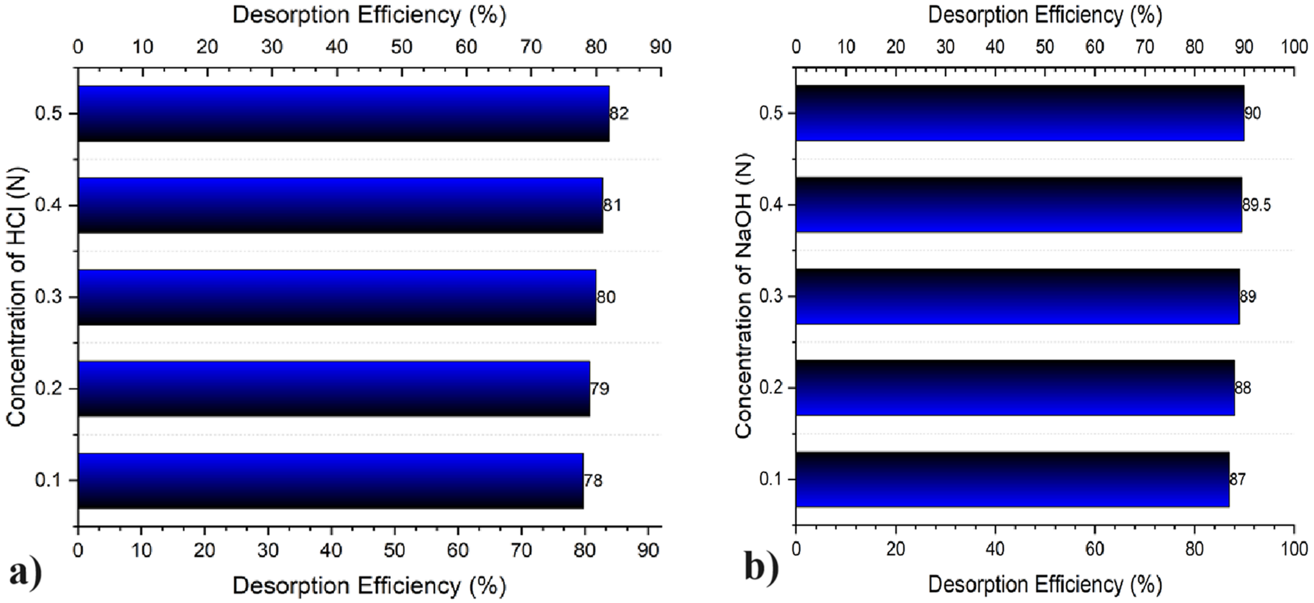

Fig. 18 Desorption efficiency for (**a**) nickel and (**b**) chromium ions

The observed peak adsorption efficiency around neutral pH suggests a strong interaction between multiple nickel species and the B-MgFe-BC functional groups. These species likely include Ni^{2+}, nickel hydroxide cations ($NiOH^+$), and even nickel dihydroxide ($Ni(OH)_2$) due to their prevalence at this pH range. This highlights the synergistic effect of various nickel forms contributing to the overall adsorption process. However, a slight decline in adsorption is observed at even higher pH values. This can be attributed to the formation of soluble nickel hydroxyl complexes. These complexes have a reduced affinity for the B-MgFe-BC surface compared to their free ionic counterparts. Their adsorption likely occurs through secondary mechanisms such as ion exchange with surface cations or hydrogen bonding with the functional groups. This delicate interplay between electrostatic attraction, competing ions, and the formation of various nickel species dictates the nuanced pH-dependent adsorption behavior observed for nickel ions on B-MgFe-BC [23].

4 Conclusion

In this extensive investigation, B-MgFe-BC was strategically employed to evaluate its effectiveness in the removal of nickel and chromium ions from solutions. Valuable insights from Fourier Transform Infrared (FTIR) analysis revealed the presence of functional groups associated with biochar, alongside the identification of M-O bonds, indicating the successful integration of MgFe into the biochar matrix. Subsequent characterizations deepened our understanding of these functional groups within the synthesized MgFe. Further analyses were conducted to validate the formation of MgFe and ascertain their interaction with the polymer matrix. Moreover, the scanning electron microscopy (SEM) examination of B-MgFe-BC unveiled a biochar matrix onto which the agglomerated MgFe-AC is attached. In-depth particle size analysis disclosed B-MgFe-BC stands out with the highest Z average, signifying a larger average particle size compared to the other materials, while BET analysis underscored a substantial surface area, suggesting that the adsorbent B-MgFe-BC is microporous in nature and has greater surface area when compared to MgFe-AC. These characteristics significantly enhance its suitability for studies in adsorption. Exploring batch adsorption studies, the emphasis was on the removal of chromium and nickel ions, revealing rapid kinetics with an efficiency greater than 70% by the 110-minute mark. The second-order kinetic model demonstrated a correlation coefficient approaching unity, highlighting the reliability of the observed kinetics. Systematic exploration of various process parameters provided a comprehensive understanding of the removal process.

The Temkin isotherm emerged as the most suitable description for the adsorption process, emphasizing the precision of the modeling. Temperature studies revealed that the adsorption of both nickel and chromium is endothermic, with peak efficiency noted at 60 °C, indicating a robust affinity between metal ions and the adsorbent. Desorption studies for chromium ions, employing a 0.5 N NaOH solution, resulted in a 90% removal, while for nickel ions 0.5 N HCl resulted in 82% removal, shedding light on the potential for regeneration. Crucially, the synthesis process embraced environmentally friendly methodologies, minimizing the use of toxic chemicals and incorporating cost-effective, magnetically separable properties as well as using biodegradable rice husk. In conclusion, the developed B-MgFe-BC emerges as a promising solution, showcasing robust adsorption properties and offering a compelling alternative for the efficient as well as sustainable elimination of chromium ions from aqueous solutions.

Supplementary Information The online version contains supplementary material available at https://doi.org/10.1007/s10450-024-00523-1.

Author contributions Conceptualization, Methodology, Writing - Original Draft: Gautham Kurup, Neeraj Krishnan, Vaishnav M. R, Roopak A. R, Validation, Supervision, Writing - Review & Editing, Supervision: K. Nithya, Asha Sathish, Selvaraju Sivamani, Aswathy S. Cheruvally : Validation, Writing - Review & Editing.

Data availability No datasets were generated or analysed during the current study.

Declarations

Ethical approval Not applicable.

Consent to participate Not applicable.

Consent to publish Not applicable.

Competing interests The authors declare no competing interests.

References

1 Al-Ghouti, M.A., Da'ana, D.A.: Guidelines for the use and interpretation of adsorption isotherm models: A review. J. Hazard. Mater. **393** (2020). https://doi.org/10.1016/j.jhazmat.2020.122383 Elsevier B.V

2 Álvarez, P., Blanco, C., Granda, M.: The adsorption of chromium (VI) from industrial wastewater by acid and base-activated lignocellulosic residues. J. Hazard. Mater. **144**(1–2), 400–405 (2007). https://doi.org/10.1016/j.jhazmat.2006.10.052

3 Amdeha, E.: Biochar-based nanocomposites for industrial wastewater treatment via adsorption and photocatalytic degradation and the parameters affecting these processes. In: Biomass Conversion and Biorefinery. Springer Science and Business Media Deutschland GmbH (2023). https://doi.org/10.1007/s13399-023-04512-2

4 Amen, R., Yaseen, M., Mukhtar, A., Klemeš J.J., Saqib, S., Ullah, S., Al-Sehemi A.G., Rafiq, S., Babar, M., Fatt C.L., Ibrahim, M., Asif, S., Qureshi K.S., Akbar M.M., Bokhari, A.: Lead and cadmium removal from wastewater using eco-friendly biochar adsorbent derived from rice husk, wheat straw, and corncob. Clean. Eng. Technol. **1** (2020). https://doi.org/10.1016/j.clet.2020.100006

5 Araújo, C.S.T., Almeida, I.L.S., Rezende, H.C., Marcionilio, S.M.L.O., Léon, J.J.L., de Matos, T.N.: Elucidation of the mechanism involved in adsorption of pb(II) onto lobeira fruit (Solanum lycocarpum) using Langmuir, Freundlich and Temkin isotherms. Microchem. J. **137**, 348–354 (2018). https://doi.org/10.1016/j.microc.2017.11.009

6 Aslibeiki, B., Varvaro, G., Peddis, D., Kameli, P.: Particle size, spin wave and surface effects on magnetic properties of MgFe2O4 nanoparticles. J. Magn. Magn. Mater. **422**, 7–12 (2017). https://doi.org/10.1016/j.jmmm.2016.08.057

7 Chai, W.S., Cheun, J.Y., Kumar, P.S., Mubashir, M., Majeed, Z., Banat, F., Ho, S.H., Show, P.L.: A review on conventional and novel materials towards heavy metal adsorption in wastewater treatment application. In *Journal of Cleaner Production* (Vol. 296). Elsevier Ltd. (2021). https://doi.org/10.1016/j.jclepro.2021.126589

8 Dang, D., Mei, L., Yan, G., Liu, W.: Synthesis of Nanoporous Biochar from Rice Husk for Adsorption of Methylene Blue. *Journal of Chemistry*, *2023*. (2023). https://doi.org/10.1155/2023/6624295

9 Dutta, D., Arya, S., Kumar, S.: Industrial wastewater treatment: Current trends, bottlenecks, and best practices. Chemosphere. **285** (2021). https://doi.org/10.1016/j.chemosphere.2021.131245

10 Ewecharoen, A., Thiravetyan, P., Nakbanpote, W.: Comparison of nickel adsorption from electroplating rinse water by coir pith and modified coir pith. Chem. Eng. J. **137**(2), 181–188 (2008). https://doi.org/10.1016/j.cej.2007.04.007

11 Goodarz Naseri, M., Ara, M.H.M., Saion, E.B., Shaari, A.H.: Superparamagnetic magnesium ferrite nanoparticles fabricated by a simple, thermal-treatment method. J. Magn. Magn. Mater. **350**, 141–147 (2014). https://doi.org/10.1016/j.jmmm.2013.08.032

12 Govindankutty, G., Hareendran, S., Sathish, A., Kamaraj, N.: Controlled functionalisation of graphene oxide using ethylene diamine: A one-pot synthesis approach for chromium sorption. Micro Nano Lett. **15**(12), 817–821 (2020). https://doi.org/10.1049/mnl.2020.0158

13 Granados-Correa, F., Jiménez-Becerril, J.: Chromium (VI) adsorption on boehmite. J. Hazard. Mater. **162**(2–3), 1178–1184 (2009). https://doi.org/10.1016/j.jhazmat.2008.06.002

14 Irfan, M., Zaheer, F., Hussain, H., Naz, M.Y., Shukrullah, S., Legutko, S., Mahnashi, M.H., Alsaiari, M.A., Ghanim, A.A.J., Rahman, S., Alshorman, O., Alkahtani, F.S., Khan, M.K.A., Kruszelnicka, I., Ginter-Kramarczyk, D.: Kinetics and Adsorption isotherms of Amine-Functionalized Magnesium Ferrite Produced using Sol-Gel Method for Treatment of Heavy metals in Wastewater. Materials. **15**(11) (2022). https://doi.org/10.3390/ma15114009

15 Jiang, C., Wang, X., Wang, G., Hao, C., Li, X., Li, T.: Adsorption performance of a polysaccharide composite hydrogel based on crosslinked glucan/chitosan for heavy metal ions. Compos. Part. B: Eng. **169**, 45–54 (2019). https://doi.org/10.1016/j.compositesb.2019.03.082

16 Khalfaoui, M., Knani, S., Hachicha, M.A., Lamine, A., Ben: New theoretical expressions for the five adsorption type isotherms classified by BET based on statistical physics treatment. J. Colloid Interface Sci. **263**(2), 350–356 (2003). https://doi.org/10.1016/S0021-9797(03)00139-5

17 Mezenner, N.Y., Bensmaili, A.: Kinetics and thermodynamic study of phosphate adsorption on iron hydroxide-eggshell waste. Chem. Eng. J. **147**(2–3), 87–96 (2009). https://doi.org/10.1016/j.cej.2008.06.024

18 Muhammad, A., Shah, H.A., A., Bilal, S.: Effective adsorption of hexavalent chromium and divalent nickel ions from water through polyaniline, iron oxide, and their composites. Appl. Sci. (Switzerland). **10**(8) (2020). https://doi.org/10.3390/APP10082882

19 Nithya, K., Sathish, A., Pradeep, K., Kiran Baalaji, S.: Algal biomass waste residues of Spirulina platensis for chromium adsorption and modeling studies. J. Environ. Chem. Eng. **7**(5), 103273 (2019). https://doi.org/10.1016/j.jece.2019.103273

20 Ntuli T.D., Mongwe T.H., Sikeyi L.L., Mkhari O., Coville N.J., Nxumalo E.N., Maubane-Nkadimeng M.S.: Removal of hexavalent chromium via an adsorption coupled reduction mechanism using olive oil derived carbon nano-onions.

Environ. Nanatechnol. Monit. Manage. **16** (2021). https://doi.org/10.1016/j.enmm.2021.100477

21 Pathak, U., Das, P., Banerjee, P., Datta, S.: Treatment of wastewater from a dairy industry using rice husk as adsorbent: Treatment efficiency, isotherm, thermodynamics, and kinetics modelling. J. Thermodyn. **2016** (2016). https://doi.org/10.1155/2016/3746316

22 Peng, X.W., Zhong, L.X., Ren, J.L., Sun, R.C.: Highly effective adsorption of heavy metal ions from aqueous solutions by macroporous xylan-rich hemicelluloses-based hydrogel. J. Agric. Food Chem. **60**(15), 3909–3916 (2012). https://doi.org/10.1021/jf300387q

23 Rafatullah, M., Sulaiman, O., Hashim, R., Ahmad, A.: Adsorption of copper (II), chromium (III), nickel (II) and lead (II) ions from aqueous solutions by meranti sawdust. J. Hazard. Mater. **170**(2–3), 969–977 (2009). https://doi.org/10.1016/j.jhazmat.2009.05.066

24 Rodriguez-Narvaez, O.M., Peralta-Hernandez, J.M., Goonetilleke, A., Bandala, E.R.: Biochar-supported nanomaterials for environmental applications. J. Industrial Eng. Chem. (Vol. **78**, 21–33 (2019). https://doi.org/10.1016/j.jiec.2019.06.008 Korean Society of Industrial Engineering Chemistry

25 Sarkar, A., Ranjan, A., Paul, B.: Synthesis, characterization and application of surface-modified biochar synthesized from rice husk, an agro-industrial waste for the removal of hexavalent chromium from drinking water at near-neutral pH. Clean Technol. Environ. Policy. **21**(2), 447–462 (2019). https://doi.org/10.1007/s10098-018-1649-5

26 Tatarchuk, T., Myslin, M., Lapchuk, I., Shyichuk, A., Murthy, A.P., Gargula, R., Kurzydło, P., Bogacz, B.F., Pędziwiatr, A.T.: Magnesium-zinc ferrites as magnetic adsorbents for cr(VI) and ni(II) ions removal: Cation distribution and antistructure modeling. Chemosphere. **270** (2021). https://doi.org/10.1016/j.chemosphere.2020.129414

27 Wang, J., Guo, X.: Adsorption kinetic models: Physical meanings, applications, and solving methods. J. Hazard. Mater. **390** (2020). https://doi.org/10.1016/j.jhazmat.2020.122156 Elsevier B.V.

28 Wang, Z., Li, Y., Wang, Z., Zhou, L.: Factors influencing the Methane Adsorption Capacity of Coal and Adsorption Heat variations. Energy Fuels. (2023). https://doi.org/10.1021/acs.energyfuels.3c02339

29 Xiang, W., Zhang, X., Chen, J., Zou, W., He, F., Hu, X., Tsang, D.C.W., Ok, Y.S., Gao, B.: Biochar technology in wastewater treatment: A critical review. In *Chemosphere* (Vol. 252). Elsevier Ltd. (2020). https://doi.org/10.1016/j.chemosphere.2020.126539

30 Yu, M., Zhu, B., Yu, J., Wang, X., Zhang, C., Qin, Y.: A biomass carbon prepared from agricultural discarded walnut green peel: Investigations into its adsorption characteristics of heavy metal ions in wastewater treatment. Biomass Convers. Biorefinery. **13**(14), 12833–12847 (2023a). https://doi.org/10.1007/s13399-021-02217-y

31 Yu, M., Zhu, B., Yu, J., Wang, X., Zhang, C., Qin, Y.: A biomass carbon prepared from agricultural discarded walnut green peel: Investigations into its adsorption characteristics of heavy metal ions in wastewater treatment. Biomass Convers. Biorefinery. **13**(14), 12833–12847 (2023b). https://doi.org/10.1007/s13399-021-02217-y

32 Zhang, Q., Zhang, D., Lu, W., Khan, M.U., Xu, H., Yi, W., Lei, H., Huo, E., Qian, M., Zhao, Y., Zou, R.: Production of high-density polyethylene biocomposites from rice husk biochar: Effects of varying pyrolysis temperature. Sci. Total Environ. **738** (2020). https://doi.org/10.1016/j.scitotenv.2020.139910